

IN-74  
176778  
P- 113

NASA Contractor Report 4012

## Polarization Modulated Ellipsometry

James L. Lauer and Norbert Marxer

GRANT NAG3-222

SEPTEMBER 1986

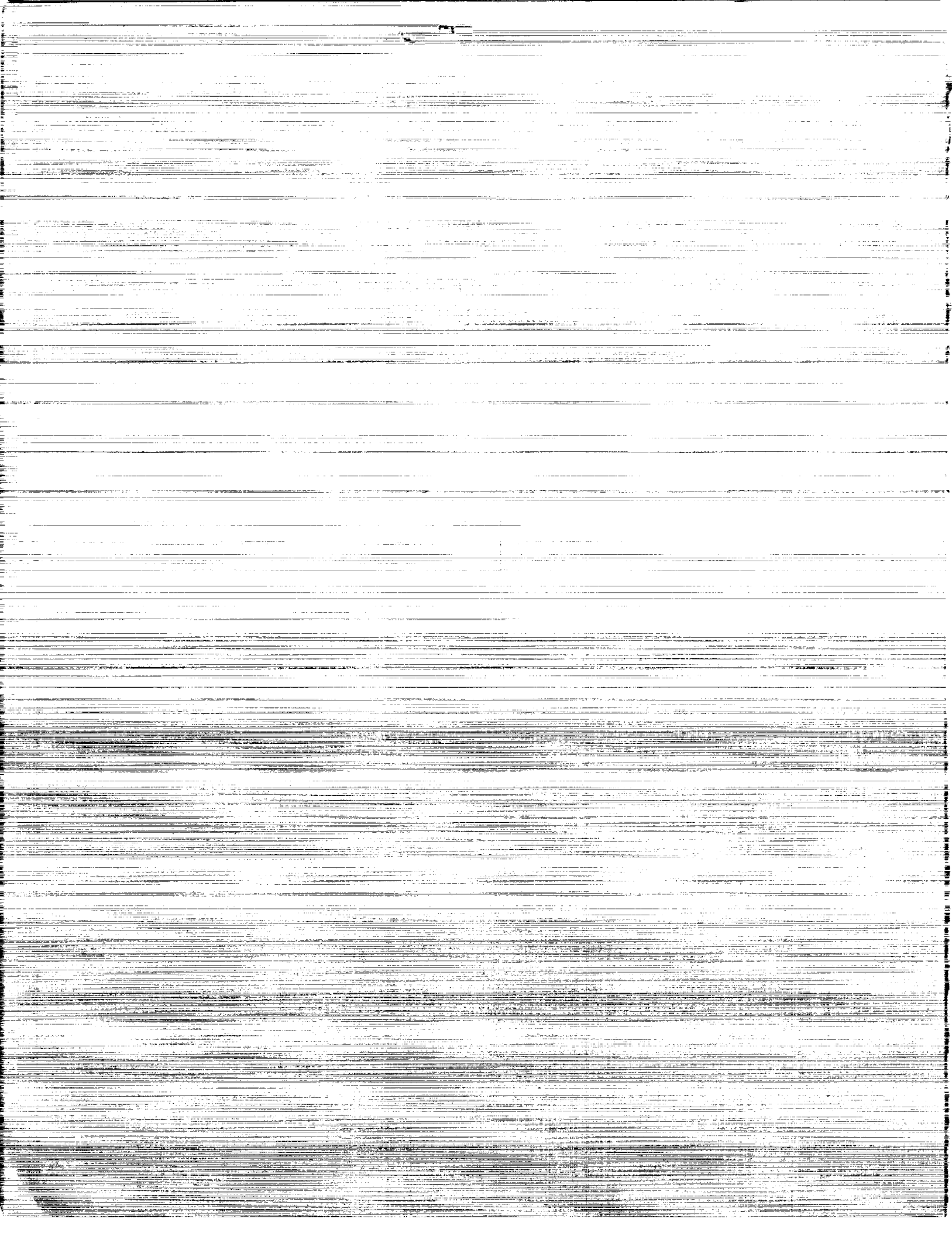
(NASA-CR-4012) POLARIZATION  
MODULATED ELLIPSOMETRY Final Report  
(Rensselaer Polytechnic Inst.)  
113 p

N93-30372

Unclass

H1/74 0176778

NASA



NASA Contractor Report 4012

# Polarization Modulated Ellipsometry

James L. Lauer and Norbert Marxer  
*Rensselaer Polytechnic Institute*  
*Troy, New York*

Prepared for  
Lewis Research Center  
under Grant NAG3-222

**NASA**  
National Aeronautics  
and Space Administration

**Scientific and Technical  
Information Branch**

1986



## SUMMARY

For the investigation of the composition and thickness of thin nonuniform films on bearing and other tribological surfaces an automated ellipsometer was built, which is extremely sensitive to relative changes in thickness and composition of surface films. These changes can be seen by scanning across the surface with 20  $\mu\text{m}$  lateral resolution. By measuring at different angles of incidence one can determine the film thickness and identify the material of the film by its complex index of refraction. For the analysis of organic layers on top of several metallic layers it was necessary to develop mathematical procedures to increase the absolute precision of the instrument.

The ellipsometer is described in detail, and the precision is discussed. The actual performance of the ellipsometer was tested on three experiments. In the first one the composition and thickness of patches of an oxide film inside a wear track were determined. In the second the thickness of a carbon overcoat sputtered on a computer disk was measured: the carbon was identified as graphitic and of random orientation. In the third the thickness of silicon oxide on top of a silicon substrate was found.

Important features of this apparatus are (i) accurate settings of the polarization stages and the angle of incidence (both automated), (ii) high precision in the determination of the ellipsometric parameters without calibration prior to an experiment and (iii) very accurate scanning modes with high spatial resolution. The instrumentation and the mathematical procedures were developed here for the first time.



# CONTENTS

	Page
SUMMARY .....	iii
1. INTRODUCTION AND HISTORICAL REVIEW .....	1
1.1 Objectives .....	1
1.2 Ellipsometry .....	2
1.2.1 Null Ellipsometers .....	4
1.2.1.1 Conventional Null Ellipsometers ....	4
1.2.1.2 Faraday-Modulated Ellipsometer ....	6
1.2.1.3 Angle of Incidence Tuning Ellipsometer .....	7
1.2.2 Photometric Ellipsometers .....	7
1.3 Summary .....	8
2. THEORY OF THIN FILMS .....	10
2.1 Bare Substrate .....	11
2.2 One Film on a Substrate .....	12
2.3 Several Films on a Substrate .....	14
3. EXPERIMENTAL SET-UP .....	16
4. MATHEMATICAL ANALYSIS OF THE ELLIPSOMETER SET-UP .....	19
4.1 PMSA Set-up .....	20
4.1.1 Mode 1 .....	21
4.1.2 Mode 2 .....	22
4.2 PMQSA Set-up .....	22
4.2.1 Mode 3 .....	22
5. COMPUTER SIMULATION .....	24
6. COMPARISON BETWEEN EXPERIMENT AND THEORY .....	29
6.1 Mode 1 .....	29
6.2 Modes 2 and 3 .....	34

	Page
7. SOME APPLICATIONS .....	38
7.1 Analysis of Wear Tracks .....	38
7.2 Thickness Measurement for a Carbon Overcoating on a Computer Disk .....	40
7.3 Silicon Oxide Film Thickness Measurement .....	55
8. DISCUSSION AND CONCLUSIONS .....	61
8.1 Ellipsometry .....	61
8.2 Summary of the Experiments .....	64
8.2.1 Wear Track Analysis .....	65
8.2.2 Carbon Coating .....	65
8.2.3 Silicon Oxide Film .....	66
8.3 Summary .....	66
LITERATURE CITED .....	68
APPENDIX A - SOME DEFINITIONS .....	71
APPENDIX B - DERIVATION OF THE MUELLER MATRICES .....	79
APPENDIX C - DESCRIPTION OF OPTICAL COMPONENTS .....	86
APPENDIX D - DESCRIPTION OF ELECTRONIC COMPONENTS .....	92
APPENDIX E - COMPUTER PROGRAMS .....	101



## CHAPTER 1

### INTRODUCTION AND HISTORICAL REVIEW

#### 1.1 Objectives

It is not yet fully understood what happens in wear tracks of lubricated bearings under elastohydrodynamic conditions. Hence, it would be desirable to find a correlation between surface structure in the wear track and time-to-failure, allowing one to understand the behavior of common lubricants and additives and to help in the design of antiscuff additives. Earlier work in our laboratory (Lauer, Fung and Jones [1]) had shown that wear tracks produced in the presence of lubricants and additives which promoted scuffing were also more reactive toward topically applied hydrochloric acid. These differences could be correlated to differences in oxidation patterns (Lauer, Marxer and Jones [2]) which were found using Auger electron spectroscopy. This technique requires ultrahigh vacuum, is slow, and for a film thickness measurement the film has to be sputtered away by ion bombardment. Because of these drawbacks we decided to use ellipsometry as our tool. With it, the film thickness and molecular composition can be found in a fast and nondestructive manner. Moreover, ellipsometry is exceedingly sensitive to surface properties, requires no vacuum and is relatively inexpensive. One disadvantage, though, is the difficulty in interpreting the measurements.

The ellipsometer built for the analysis was also used for a feasibility study; the question was whether it is possible to

determine the film thickness of a carbon overcoat sputtered onto a computer disk which consists of several metallic layers. The carbon overcoat serves both as lubricant and protective layer. To determine the thickness and structure of the carbon overcoat nondestructively would be very useful in elucidating the performance of the disk in normal operating conditions.

The last investigation described in this thesis is the film thickness measurement of a protective silicon oxide ( $\text{SiO}_2$ ) layer on top of a silicon wafer.

## 1.2 Ellipsometry

Ellipsometers are not principally new instruments. Already in 1890 (Rayleigh [3], Drude [4,5]) it was realized that extremely thin (a few Å) films could be detected by analyzing the polarization state of light before and after reflection from a surface. But especially in the last twenty years, because of the availability of lasers, fast electronics, computers and the increased interest in surface properties, many different types of ellipsometers have been built. They all determine the complex number  $\rho$  [Eq.(1.1):

$$\rho \equiv \frac{\rho^{\parallel}}{\rho^{\perp}} = \frac{E_f^{\parallel}/E_i^{\parallel}}{E_f^{\perp}/E_i^{\perp}} \equiv \tan \psi e^{i\Delta} \quad (1.1)$$

where  $\rho^{\parallel}$  and  $\rho^{\perp}$  are the complex reflection coefficients for light polarized parallel and perpendicular to the plane of incidence,  $E_i^{\parallel}$ ,  $E_f^{\parallel}$ ,  $E_i^{\perp}$  and  $E_f^{\perp}$  are the complex electric field vector components in the phasor representation before and after reflection from the surface in

the direction parallel and perpendicular to the plane of incidence and  $\psi, \Delta$  are the two so-called ellipsometric parameters. The quantity  $\rho$  is related to the properties of the surface, from which the light is reflected.

If the light is reflected from a bare substrate  $\rho$  will be a function of the refractive index of the medium  $n$  ( $= 1.000$  for air), the refractive index of the substrate and the angle of incidence. A measurement of  $\rho$  at a known angle of incidence allows one to find the refractive index of the substrate. Similarly for a film covered sample the measured  $\rho$  will depend on the refractive indices of the medium, film and substrate, on the film thickness, wavelength and angle of incidence. By measuring  $\rho$  at one or several angles of incidence the unknowns can be found.

But the success of a calculation depends critically on the choice of a proper model for the surface. Usually the surface is represented by planar layers with a constant isotropic refractive index inside each layer. The question is then, whether contamination layers on the surface or small transition layers between layers can be neglected, whether the variation of the refractive index inside a layer can be ignored (e.g., King and Downs [6], Charmet and Gennes [7]), and whether anisotropy, stresses, etc. have a negligible effect. Another problem involves surface roughness which can affect  $\rho$ , but it is not yet known exactly how (Smith [8], Blanco, McMarr and Vedam [9], Vorburger and Ludema [10]). To have some confidence in the calculation it is therefore best to check the results with information obtained with other techniques.

Many ellipsometers based on different principles and with special features, have been built recently. I give here only a very brief description of some existing ellipsometers (see, for example, Azzam and Bashara [11] for more details).

The ellipsometers can be divided into two main categories. The first are the null ellipsometers, where the azimuths of the optical elements are set such that the light intensity (or the fundamental frequency part of the intensity for a modulated beam) becomes zero at the detector. The second category comprises photometric ellipsometers which measure intensities as a function of the azimuth settings of the different optical components and/or the retardance of the compensator. From the settings of the azimuths in the null instrument and from the intensities in the photometric ellipsometer the complex  $\rho$  can be found.

#### 1.2.1 Null Ellipsometers

##### 1.2.1.1 Conventional Null Ellipsometry

The most widely used ellipsometers are the conventional null ellipsometers which use a polarizer P, a compensator C (e.g., quarter-wave plate), and an analyzer A (see Figure 1.1). There are two set-ups possible: PCSA or PSCA where S stands for the sample, and the order of the letters gives the order in which the light beam traverses the components. In both set-ups one of the components is held at a fixed azimuth and the azimuths of the two other components are adjusted such that the light intensity on the detector is zero.

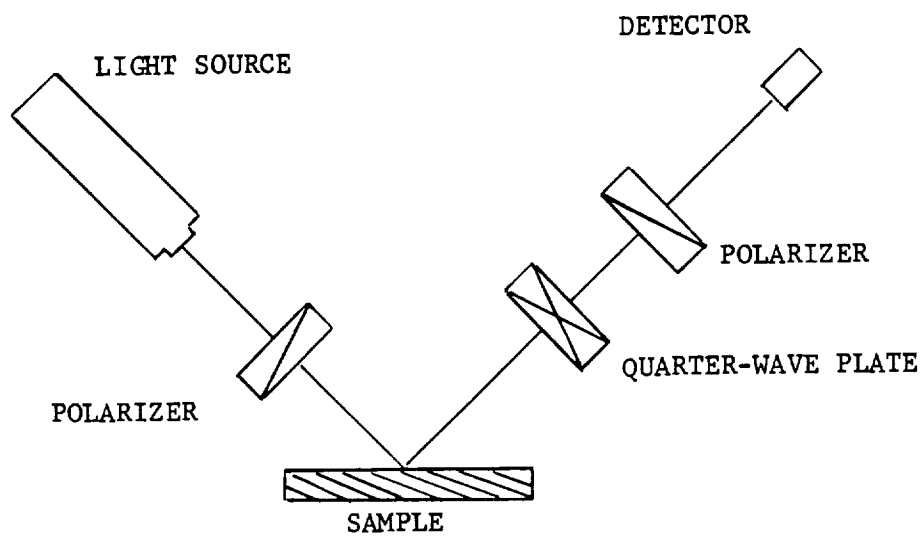


Figure 1.1 Typical Ellipsometer Set-up

For the PSCA ellipsometer the linearly polarized light which is incident on the sample will become elliptically polarized, because its electric field vector components parallel and perpendicular to the plane of incidence usually experience different amplitude- and phase-changes upon reflection. The ellipsometer got its name from the fact that it allows one to find the shape and orientation of this polarization ellipse. With a quarter-wave plate (which introduces a phase difference of 90 degrees for the electric field vector components parallel and perpendicular to the fast axis of the quarter-wave plate) the light is made linearly polarized again and the light intensity reaching the detector can be made zero (null) with a second polarizer which is usually called analyzer. From the settings of the polarizer, quarter-wave plate and analyzer azimuths, which produce a null, the quantity  $\rho$  can be calculated.

The null can be found visually or more precisely with the help of a half-shade device, Faraday modulators, or a fit of a parabola to the intensity close to the minimum. It is also possible to replace the mechanical rotation stages by all electro-optical devices. But the principle is always the same; the changes affect only the ease, precision (e.g., Merkt [12]) and speed of a measurement (e.g., Winterbottom [13]).

#### 1.2.1.2 Faraday-Modulated Ellipsometer

In Faraday-modulated ellipsometry (Monin and Boutry [14]) the compensator is replaced by an optical rotator. The rotator employing the Faraday magneto-optic effect moves the plane of

polarization sinusoidally back and forth and by adjusting the polarizer or the analyzer the fundamental frequency component of the light intensity on the detector can be made zero. A measurement at two polarizer azimuths gives  $\rho$ .

#### 1.2.1.3 Angle of Incidence Tuning Ellipsometer

With this method the angle of incidence and the polarizer azimuth are set so that the intensity on the detector is zero. The method is based on the fact that the phase change of light upon reflection depends on the angle of incidence. The angle is adjusted so that for two reflections (e.g., O'Bryan [15], Marchand and Wrobel [16])  $\rho$  is real. Then the light after two reflections is linearly polarized and can be extinguished with a polarizer without the use of a compensator.

#### 1.2.2 Photometric Ellipsometers

The photometric ellipsometers record the intensity as a function of the azimuths of the optical components (P,C,A) or the retardance of the compensator (Moritani, Okuda, Kubo and Naki [17]). In a static photometric ellipsometer the intensity is measured at various azimuths of the optical components and  $\rho$  can be calculated (e.g., Roesler [18] in the infrared). Using this design a time resolution of 100 ns has been reported (Jellison and Lowndes [19]). In a dynamic photometric ellipsometer one or more optical components are rotated continuously and a Fourier transform of the intensity versus time curve gives  $\rho$  (e.g., Aspnes [20], Chandler-Horowitz and

Candela [21], Stobie, Rao and Dignam [22]). Many kinds of operations are possible where the optical set-up (PCSA, PSCA or PSA) and/or the elements to be turned are different. A very high accuracy has been claimed (Candela and Chandler-Horowitz [23]) surpassing any calibration standards available.

Each ellipsometer has its own advantages and the selection of one depends on the application, whether one needs high accuracy (one of the dynamic photometric ellipsometers), simple operation as in an industry environment (automated conventional ellipsometer), spectroscopic information (ellipsometer without a compensator) or ultrafast speed (static photometric ellipsometer as described by Jellison and Lowndes [19]).

### 1.3 Summary

The ellipsometer we built is a Faraday-modulated ellipsometer based on the design by Monin and Boutry [14]. The same principle has been used by Sullo and Moore [24] and Sullo [25] in measuring the refractive index of gradient index fibers. The advantage of this design is that no compensator or quarter-wave plate is used and that the modulation technique makes a very precise determination of a null possible.

When I started my work on ellipsometry we had a copy of Sullo's ellipsometer; but it turned out that major changes were necessary to adapt it for our studies. Because the instrument developed has some unique features which are not yet published in the literature, the main part of the thesis is devoted to the



description of the ellipsometer. The experiments performed with it are discussed only briefly, because they have already been described in detail elsewhere (Lauer, Marxer and Jones [26], Lauer and Marxer [27]).

In Chapter 2 the calculation of refractive indices and film thicknesses are given for bare substrates, a single film on a substrate, and multilayer structures. Chapter 3 contains a description of our instrumentation. In Chapter 4 a theoretical analysis gives the formulas which relate the azimuths of the different optical components to  $\rho$ . Possible errors, the effect of imperfect optical components and the settings for highest accuracy are analyzed in Chapter 5 with computer simulations. In Chapter 6 the actual performance of the ellipsometer is compared to the theory and deviations are discussed. Chapter 7 contains a summary of the experiments which were the actual reason for building this instrument and the final chapter, Chapter 8, summarizes the overall performance of the ellipsometer and the results of our experiments.

Most of the experimental and theoretical work is described in more detail in the appendices.

## CHAPTER 2

### THEORY OF THIN FILMS

In ellipsometry the change of the polarization state of light upon reflection from a surface is measured, and from these measurements optical constants and film thicknesses can be calculated using appropriate models. Upon reflection both the electric field vector parallel and perpendicular to the plane of incidence are modified in their amplitude and their phase. This process is described by Eqs.(2.1) and (2.2).

$$e_f^{\parallel} = \rho_{\parallel} e_i^{\parallel} \quad (2.1)$$

$$e_f^{\perp} = \rho_{\perp} e_i^{\perp} \quad (2.2)$$

where the final and initial complex electric field vectors are linearly related to each other by the (complex) reflection coefficients  $\rho_{\parallel}$ ,  $\rho_{\perp}$ . The complex quantity which is measured with an ellipsometer is

$$\rho \equiv \frac{\rho_{\parallel}}{\rho_{\perp}} \equiv \tan \psi e^{i\Delta} \quad (2.3)$$

If we write the complex reflection coefficients  $\rho_{\parallel} = r_{\parallel} e^{i\Delta_{\parallel}}$  and  $\rho_{\perp} = r_{\perp} e^{i\Delta_{\perp}}$  then  $\psi$  and  $\Delta$ , the two real ellipsometric parameters, are defined in the following way:

$$\tan \psi = \frac{r_{\parallel}}{r_{\perp}} \quad (2.4)$$

$$\Delta = \Delta_{\parallel} - \Delta_{\perp} \quad (2.5)$$

The whole field of ellipsometry consists in measuring and interpreting these two parameters.

In the following we discuss only the simple case of planar multilayer isotropic media. Except in the case of a bare substrate, no formula can be given to calculate directly optical constants or film thicknesses from the ellipsometric parameters and much effort went into deriving sophisticated techniques to calculate them (e.g., Yoriome [28], Charlot and Maruani [29], McCrackin [30], see also Appendix E), but they are usually designed to be used in special cases only (e.g., transparent film).

The starting point for the calculations are the Fresnel coefficients, which give the amplitude- and phase-change of light upon reflection from and transmission through an interface. These coefficients can be derived from Maxwell's equations (see for example Jackson [31]) and are given along with the chosen coordinate systems in Appendix A.

## 2.1 Bare Substrate

When light is reflected from a bare substrate  $\rho$  is given by Eq. (2.6):

$$\rho = \frac{r_{01}^{\parallel}}{r_{01}^{\perp}} \quad (2.6)$$

where  $r_{01}^{\parallel}$  and  $r_{01}^{\perp}$  are the Fresnel reflection coefficients at the medium/substrate interface for light polarized parallel and perpendicular to the plane of incidence. From the measured  $\rho$  the complex

refractive index  $\hat{n}_s$  of the substrate can be calculated with Eq. (2.7) (see Azzam and Bashara [11])

$$\hat{n}_s = n_M \cdot \sin \alpha \left( 1 - \frac{4\rho}{(1+\rho)^2} (\sin \alpha)^2 \right)^{1/2} \quad (2.7)$$

where  $n_M$  is the refractive index of the medium (always air in our experiments) and  $\alpha$  is the angle of incidence.

## 2.2 One Film on a Substrate

When light is reflected from a film covered substrate, and we take multiple reflections into account (see Figure 2.1), we get Eq. (2.8) for the reflection coefficient  $\rho^{\parallel}$  for light polarized parallel to the plane of incidence (and an analog expression for  $\rho^{\perp}$ ); Azzam and Bashara [5],

$$\rho^{\parallel} = \frac{r_{01}^{\parallel} + r_{12}^{\parallel} e^{i2\gamma}}{1 + r_{01}^{\parallel} r_{12}^{\parallel} e^{i2\gamma}} \quad (2.8)$$

where  $r_{01}^{\parallel}$  and  $r_{12}^{\parallel}$  are the Fresnel reflection coefficients at the medium/film interface and the film/substrate interface, respectively, and  $\gamma$  is defined by Eq. (2.9):

$$\gamma = \frac{2\pi d}{\lambda} n_F \cos \alpha_F \quad (2.9)$$

where  $d$  is the film thickness,  $\lambda$  is the wavelength,  $n_F$  is the refractive index of the film and  $\alpha_F$  is the angle between the direction of propagation of the light inside the film and the surface normal if the film is transparent.

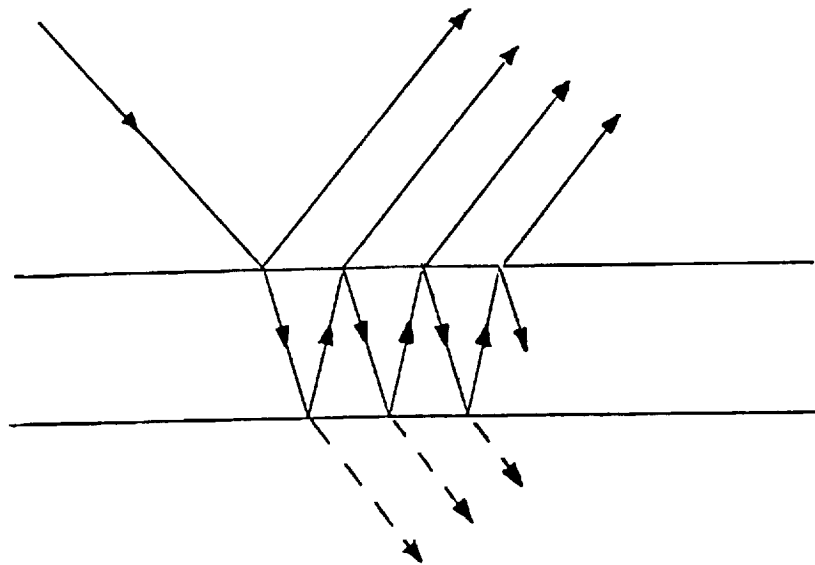


Figure 2.1 Multiple Reflections in a Thin Film on a Substrate

For an absorbing film this angle will be complex and has no physical meaning. But  $\cos \alpha_F$  can be easily calculated using Snell's law [Eq.(2.10)]

$$n_M \sin \alpha = n_F \sin \alpha_F \quad (2.10)$$

and the fact that

$$\cos \alpha_F = \left(1 - (\sin \alpha_F)^2\right)^{1/2} \quad (2.11)$$

The complex angle causes no problem as long as we select the correct solution of the square root in Eq.(2.11). There is a mathematical description which gives a real angle even for absorbing films, but then the refractive index will depend on the angle of incidence (e.g., Vasicek [32]) even for isotropic materials.

There is a different sign in the exponent of Eq.(2.8) compared to Azzam and Bashara [11], because we chose the time dependence of a plane wave differently ( $e^{-i\omega t}$  versus  $e^{i\omega t}$ , see Appendix A).

The relationship between  $\rho^{\parallel}$  and  $\rho^{\perp}$  and the experimentally determined  $\rho = \tan \psi e^{i\Delta}$  is

$$\rho = \frac{\rho^{\parallel}}{\rho^{\perp}} \quad (2.12)$$

### 2.3 Several Films on a Substrate

For several films  $\rho^{\parallel}$  and  $\rho^{\perp}$  are calculated first for the lowest interface with Eq.(2.8) using the appropriate refractive indices and the angles of incidence which are again found using Snell's

law [Eq.(2.10)]. Then we work up from the second lowest interface up to the surface using Eq.(2.8) for both directions of polarization where the Fresnel reflection coefficients are replaced by the reflection coefficients  $\rho^{\parallel}$ ,  $\rho^{\perp}$  calculated for the lower lying films. Equation (2.12) Equation (2.12) then relates the theory and the experiment.

Before the availability of computers the analysis of more than one film was very time consuming, and for the analysis of one film often a thin film approximation (Drude [4]) was used. The above given derivation is quite simple and it is astonishing that much more difficult procedures were used by some (Vasicek [32]).

The program `elli.go` we wrote allows the calculation of any imaginable combination of refractive indices and film thicknesses of up to fifty films. But because of experimental uncertainty the analysis of fifty films does not make sense except in the case where the many films are used to approximate a refractive index slowly changing in the direction of the surface normal. Some aspects of the program are described briefly in Appendix E.

## CHAPTER 3

### EXPERIMENTAL SET-UP

I give here only a brief description of the experimental set-up. More information on the optical and electronic components can be found in the Appendices C and D, respectively. Figure 3.1 shows a schematic of the instrument.

Light from a HeNe laser is polarized by a linear polarizer with the plane of polarization at an angle  $\beta$  (all angles are measured counterclockwise, when looking towards the incoming beam, starting from the plane of incidence). Then it goes through a modulator, which consists of a solenoidal coil with a special Faraday glass at its axis. By driving the coil with an AC current (frequency  $f$  is typically 500 Hz) of approximately 0.5 ampere, we obtain light whose plane of polarization is oscillating around  $\beta$  by approximately one degree. Then the linearly polarized light passes through a quarter-wave plate, is reflected from a sample surface and becomes elliptically polarized in the process, goes through a second polarizer (called analyzer), some lenses, which give us the wanted spatial resolution (20  $\mu\text{m}$ ), and finally strikes the photodiode detector. For some of the measurements the lenses and/or the quarter-wave plate were removed.

Because we modulate the plane of polarization, making a precise nulling possible, the light intensity at the detector will have a fundamental frequency component and higher harmonics superimposed on a constant intensity. The output of the light detector is connected to the input of a lock-in amplifier, which produces a



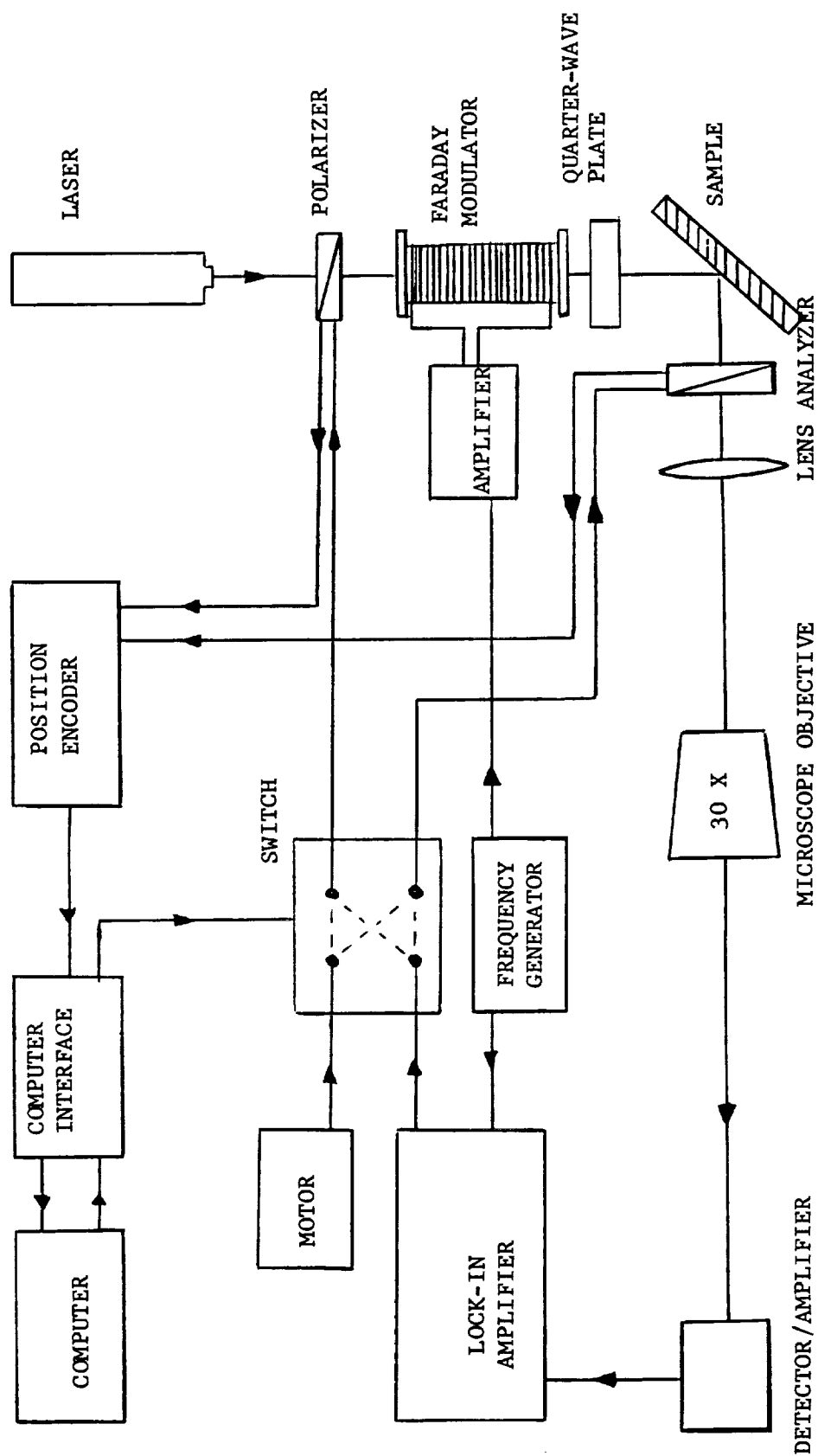


Figure 3.1 Schematic of the Ellipsometer

voltage proportional to the intensity at the fundamental frequency  $I(f)$ . This voltage is amplified and connected either to the polarizer or analyzer and will rotate the stage until  $I(f)$  is zero.

We can move the sample in the x- and y-directions parallel to the surface for scans with motor-driven stages. The polarizer and analyzer can also be connected to a DC motor and their angular position can be determined electronically with a  $.01^\circ$  precision using specially built counter boards.

The angle of incidence is variable from 25 degrees up to approximately 80 degrees using a stepping motor. To have an angle of incidence which can be changed quickly and reproducibly is very convenient in multiple angle of incidence measurements and important in many measurements in which a particular angle of incidence should be used for maximum precision.

A computer can control the different modes of operation. These different modes will be discussed in the next chapter.

## CHAPTER 4

### MATHEMATICAL ANALYSIS OF THE ELLIPSOMETER SET-UP

For a mathematical analysis of our experimental set-up, it is convenient to represent the polarization state of light by a Stokes vector and the optical components and the sample by Mueller matrices. The polarization state of light after passing through some optical components is then calculated by multiplying the corresponding matrices with the initial Stokes vector. The definition of the Stokes vector, the Mueller matrices and the method of deriving them are contained in Appendix B.

Because the modulation we apply is small (approximately one degree), the sine and cosine in the modulation matrix can be expanded [see Eq.(4.1)] and the constant part, the fundamental frequency component and the second harmonic of the intensity can be calculated:

$$M = \begin{bmatrix} 1 & 0 & 0 & 0 \\ 0 & \cos(2\mu_0 \sin \omega t) & -\sin(2\mu_0 \sin \omega t) & 0 \\ 0 & \sin(2\mu_0 \sin \omega t) & \cos(2\mu_0 \sin \omega t) & 0 \\ 0 & 0 & 0 & 0 \end{bmatrix} \approx \begin{bmatrix} 1 & 0 & 0 & 0 \\ 0 & (1 - \mu_0^2) - \mu_0^2 \cos 2\omega t & -2\mu_0 \sin \omega t & 0 \\ 0 & 2\mu_0 \sin \omega t & (1 - \mu_0^2) - \mu_0^2 \cos 2\omega t & 0 \\ 0 & 0 & 0 & 1 \end{bmatrix} \quad (4.1)$$

Our electronics locks in at the fundamental frequency and turns one of the optical elements (polarizer or analyzer) making the intensity at the fundamental frequency zero. In this way we obtain an equation, which relates the azimuth angles of the various optical elements to  $\psi$  and  $\Delta$ .

There were several reasons which led us to the chosen set-up PM(Q)SA (where P stands for polarizer, M for modulator, Q for quarter-wave plate, S for sample, A for analyzer, and the bracket around Q indicates that the quarter-wave plate was not always used).

A polarizer must be at the beginning and an analyzer at the end of the optical path. In order to obtain high spatial magnification, it is advantageous to get the lenses as close as possible to the sample. For this reason all the elements except the analyzer are placed in front of the sample. Then there remains the choice, whether the quarter-wave plate should be between the polarizer and the modulator or between the modulator and the sample. The second set-up was chosen because this set-up makes it possible to determine  $\Delta$  independently of  $\psi$ , whereas the first one does not. We will not discuss the detailed calculations for all the possible set-ups, but only the ones for the PMSA and PMQSA set-ups, which turned out to be the most useful.

#### 4.1 PMSA Set-up

The quarter-wave plate is the component which introduces the largest error in the experimental determination of  $\psi$  and  $\Delta$ . That is why it is best to eliminate it from the set-up at all (see Monin and Boutry [14]).

A calculation of the intensity of light at the fundamental frequency after passing through the PMSA set-up gives,

$$I(f) \propto \sin 2\beta (\cos 2\psi - \cos 2\alpha) + \cos 2\beta \sin 2\psi \cos \Delta \sin 2\alpha \quad (4.2)$$

and setting it equal to zero leads to Eq.(4.3) (see also Monin and Boutry [14], who derived the same equation in a different way),

$$\tan 2\beta = \frac{2 \cos \Delta \tan \psi \tan \alpha}{(\tan \psi)^2 - (\tan \alpha)^2} \quad (4.3)$$

where  $\beta$  is the polarizer azimuth and  $\alpha$  is the analyzer azimuth.

#### 4.1.1 Mode 1

If we rotate the polarizer for example, the analyzer in the feedback loop will be rotated according to Eq.(4.3). By recording many (analyzer, polarizer)-pairs and performing a least square fit  $\psi$  and  $\Delta$  and possible constant offsets in the azimuth readings of the polarizer and analyzer can be determined very accurately. We call this mode of operation mode 1. The curve fitting procedure is described in Appendix E (Program pd.go) and an experimental verification of Eq.(4.3) and a discussion of possible errors is given in Chapter 6.

We have to mention that for  $\cos \Delta = 0$  the analyzer will lock in at an azimuth  $\alpha = \psi$  independent of  $\beta$ . Moreover, because  $\cos \Delta$  is determined, the measured  $\Delta$  will have a relatively large error when  $\cos \Delta$  is close to  $\pm 1$ . The measured  $\cos \Delta$  gives two solutions for  $\Delta$  and it is impossible to tell which one is the correct one without using a quarter-wave plate or having some additional knowledge about the sample.

#### 4.1.2 Mode 2

An important feature of Eq.(4.3) is the fact that, by setting the polarizer azimuth  $\beta$  equal to 45 degrees, the analyzer (in the feed-back loop) automatically sets itself to  $\alpha = \psi$  [Eq.(4.4)],

$$\alpha = \psi + n \cdot 180^\circ \quad n = 0, \pm 1, \pm 2. \quad (4.4)$$

This fact can be used to find  $\psi$  independently of  $\Delta$ , and was extensively used when scanning across a surface. This mode of operation is called mode 2.

With the PMSA set-up it is not possible to determine  $\Delta$  in a similar way. To do that a quarter-wave plate has to be inserted between the modulator and the sample.

#### 4.2 PMQSA Set-up

For the PMQSA set-up a similar analysis as for the PMSA set-up above leads to Eq.(4.5), which relates the azimuths of the optical components to  $\psi$  and  $\Delta$ ,

$$\begin{aligned} \cos 2\tau \sin(2\tau - 2\beta)[\cos 2\psi - \cos 2\alpha] = \\ \sin 2\alpha \sin 2\psi [\cos \Delta \sin 2\tau \sin(2\tau - 2\beta) + \sin \Delta \cos(2\tau - 2\beta)] \end{aligned} \quad (4.5)$$

where  $\tau$  is the azimuth of the quarter-wave plate (angle between the plane of incidence and the fast axis of the quarter-wave plate). We used only one feature of this equation in our work.

##### 4.2.1 Mode 3

By setting  $\tau$  equal to 45 degrees and  $\alpha$  such that  $\sin 2\alpha \neq 0$  [left side of Eq.(4.5) is zero and right side is nonzero] we get Eq.(4.6),

$$\Delta = 2\beta + 90^\circ + n \cdot 180^\circ \quad n = 0, \pm 1, \pm 2 \dots \quad (4.6)$$

This mode of operation, called mode 3, was used when we wanted to obtain a  $\Delta$  versus position curve, or when  $\Delta$  was close to 180 degrees and, therefore, difficult to determine precisely using the PMSA mode.

An error analysis of this set-up is also given in Chapter 6.

## CHAPTER 5

### COMPUTER SIMULATION

The mathematical analysis given in the last chapter is performed assuming ideal optical components. With imperfect components a calculation becomes tedious and the final formulas are too complicated to be useful. The high spatial resolution required forced us to use film polarizers, which have a somewhat larger extinction ratio (ratio between the amount of light transmitted when two polarizers are crossed and the one when the two polarizers have their transmission axes parallel) than calcite polarizers. The laser delivered polarized light and the intensity change caused when turning the polarizer could also adversely influence the performance of the ellipsometer. The quarter-wave plates are also known to introduce errors.

To study all these effects the program lock.go which simulates the operation of the ellipsometer (see Appendix E) was written. Some of the conclusions are given below.

1. Because at least an extinction coefficient of  $2 \cdot 10^{-3}$  (much better ones are commercially available) is necessary to cause a detectable deviation from the ideal behavior for the PMA set-up and, moreover, our ellipsometer showed no such deviations, we assumed for our calculations that our film polarizers were ideal with a zero extinction ratio.
2. If the laser delivers a small (but within the experimental uncertainty possible) amount of unpolarized or circularly polarized light, the performance is not affected at all (PMA).



3. A good choice of the analyzer azimuth  $\alpha$  can lead to a high signal-to-noise ratio in the PMQSA set-up.

We want to illustrate this in the following for  $\psi = 22.95$  and  $\Delta = 184.00$  (i.e., silicon oxide on silicon) in the PMQSA set-up. In deriving Eq.(4.5) in Chapter 4 assuming ideal optical components we had to set  $\tau = 45$  degrees and  $\alpha$  such that  $\sin 2\alpha$  was nonzero.

But to get the best performance, the constant (DC) component of the light intensity  $[I(\text{DC})]$  should be small, and the change of the intensity (e.g.,  $\frac{\partial I(f)}{\partial \beta}$ ) at the fundamental frequency with the azimuth of the stage, which is in the feedback loop, should be large so that a small deviation from the correct position gives a large signal to drive it back. Figure 5.1 contains a plot of  $I(\text{DC})$  and  $\partial I(f)/\partial \beta$ . The units given are arbitrary, but for all plots the baseline is equal to zero. The change of  $\partial I(f)/\partial \beta$  with  $\alpha$  is not that great, but  $I(\text{DC})$  has a very small value (approximately 0.00016) in these arbitrary units at  $\psi = 22.94$ . The obvious choice for  $\alpha$  from this analysis is therefore  $\alpha = 22.94$ .

4. An imperfect quarter-wave plate can have considerable influence in the precision of a measurement:

There is another reason to choose  $\alpha = 22.94$  in the example above. Assuming perfect components, Eq.(4.5) of Chapter 4 lets us find  $\Delta$  from  $\beta$  independent of  $\alpha$  as long as  $\sin 2\alpha$  is nonzero. This is not true in the case of an imperfect

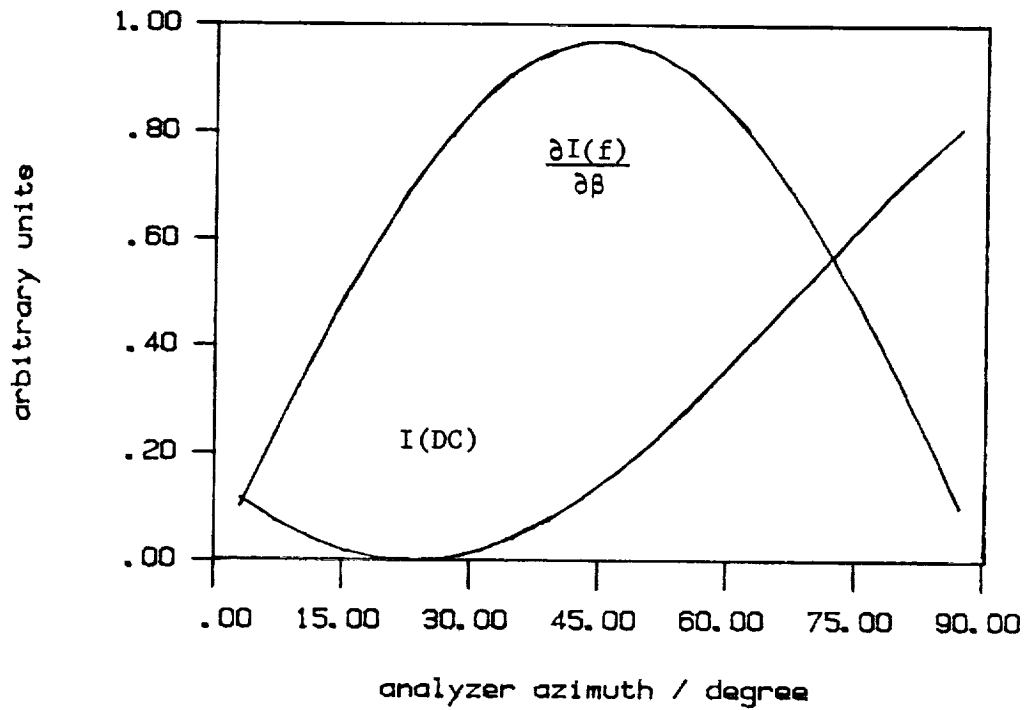


Figure 5.1 Theoretical DC Intensity and  $\frac{\partial I(f)}{\partial \beta}$  Versus Analyzer Azimuth in the PMQSA Set-up (Mode 3) with  $\psi = 22.95$  and  $\Delta = 184.00$ . The units of the ordinate are arbitrary

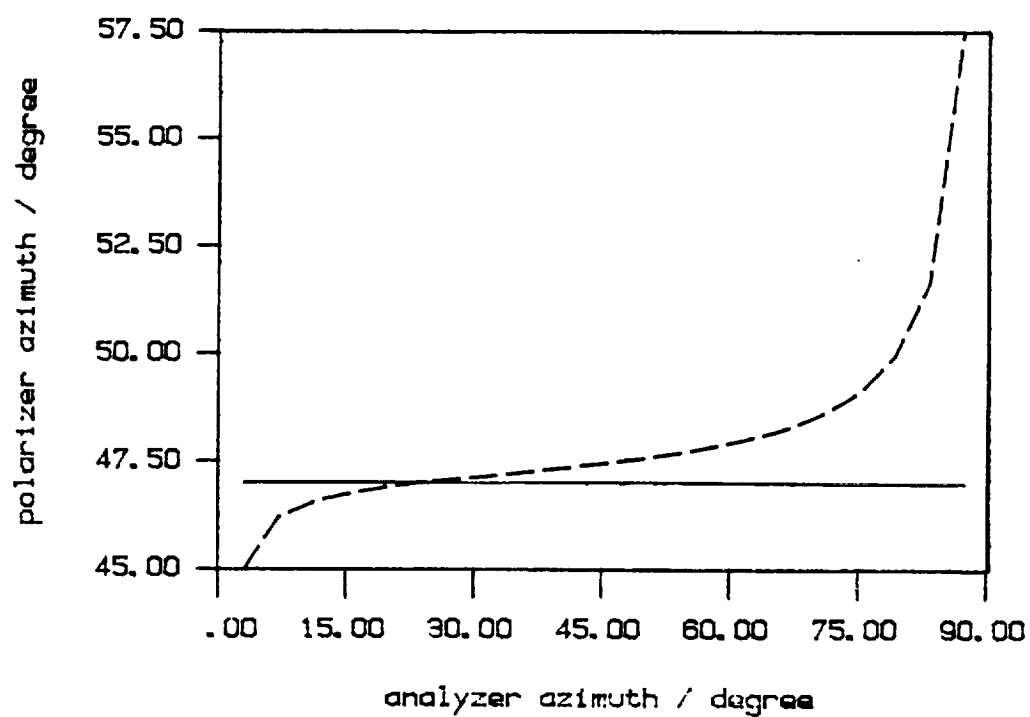


Figure 5.2 Theoretical Polarizer Azimuth Versus Analyzer Azimuth for an Ideal (—) and an Imperfect (---) Quarter-Wave Plate

quarter-wave plate. Figure 5.2 shows the polarizer azimuth at which the ellipsometer locks in for a perfect quarter-wave plate (retardance equals 90 degrees) and a quarter-wave plate with a retardance of 89 degrees. It can be clearly seen that using the ideal quarter-wave plate the theory is confirmed ( $\beta = 47$  degrees independent of the analyzer azimuth), whereas the imperfect quarter-wave plate gives the true solution only if we set  $\alpha$  close to 22.94 degrees. The change of  $\beta$  with  $\alpha$  is 0.024 deg/deg. That means that for a desired precision of 0.01 degrees  $\alpha$  should be chosen between 22.5 and 23.5 degrees approximately.

Many other checks and error estimates are possible and were performed, but not mentioned in more detail here. To arrive at the same conclusions without the help of a computer would be an extremely time-consuming task.

## CHAPTER 6

### COMPARISON BETWEEN EXPERIMENT AND THEORY

In Chapter 4 the mathematical analysis gave equations relating the azimuths of the different optical elements and the ellipsometric parameters  $\psi$  and  $\Delta$ . In Chapter 5 the influence of imperfect components was studied, and the choice of the best setting of the analyzer azimuth to minimize the effect of an imperfect quarter-wave plate when operating the ellipsometer in mode 3 was discussed.

In this chapter we want to show how well the equations derived in Chapter 4 agree with the experimental curves we get from our ellipsometer. The first part is the test of mode 1 (as defined in Chapter 4), which allows very precise determination of  $\psi$  and  $\Delta$  using the curve fitting procedure. The second part will check the performance of mode 2 and 3, in which  $\psi$  and  $\Delta$  can be determined independently of each other.

#### 6.1 Mode 1

To test Eq.(4.3) which relates the polarizer and analyzer azimuth for given  $\psi$  and  $\Delta$ , we can compare the measured  $(\alpha_m, \beta_m)$ -curves (corrected for offset) and the calculated curves  $(\alpha_m, \beta_c) =$

$$\left( \alpha_m, \frac{1}{2} \tan^{-1} \left( \frac{2 \cos \Delta \tan \psi \tan \alpha_m}{(\tan \psi)^2 - (\tan \alpha_m)^2} \right) \right). \text{ We show two plots of } \beta_m - \beta_c$$

versus  $\alpha_m$  for two examples having quite different  $\psi$  and  $\Delta$ : the first is a silicon substrate with a 3 nm silicon oxide film at an angle of incidence of 69.90 (Figure 6.1), the second is a carbon overcoated computer disk (see Chapter 7, Section 7.2) at an angle of incidence of 57.99° (Figure 6.2).

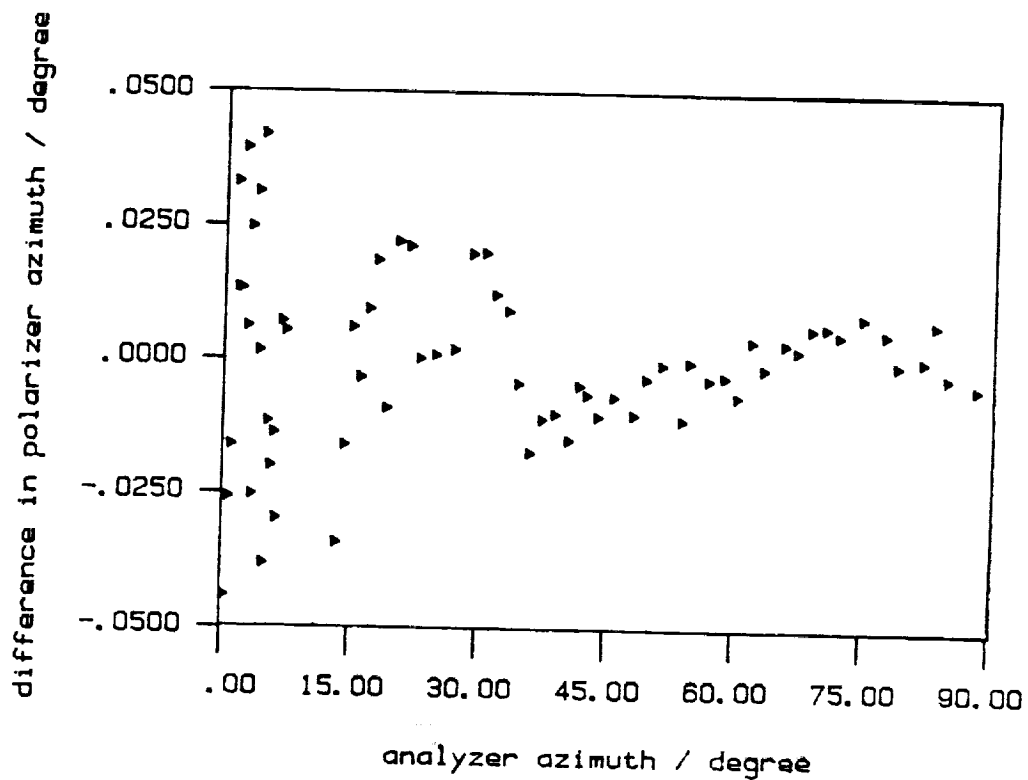


Figure 6.1 Difference Between Measured and Calculated Polarizer Azimuth Versus Analyzer Azimuth for a 3 nm Thick Silicon Oxide Film on a Silicon Substrate at an Angle of Incidence of  $69.90^\circ$

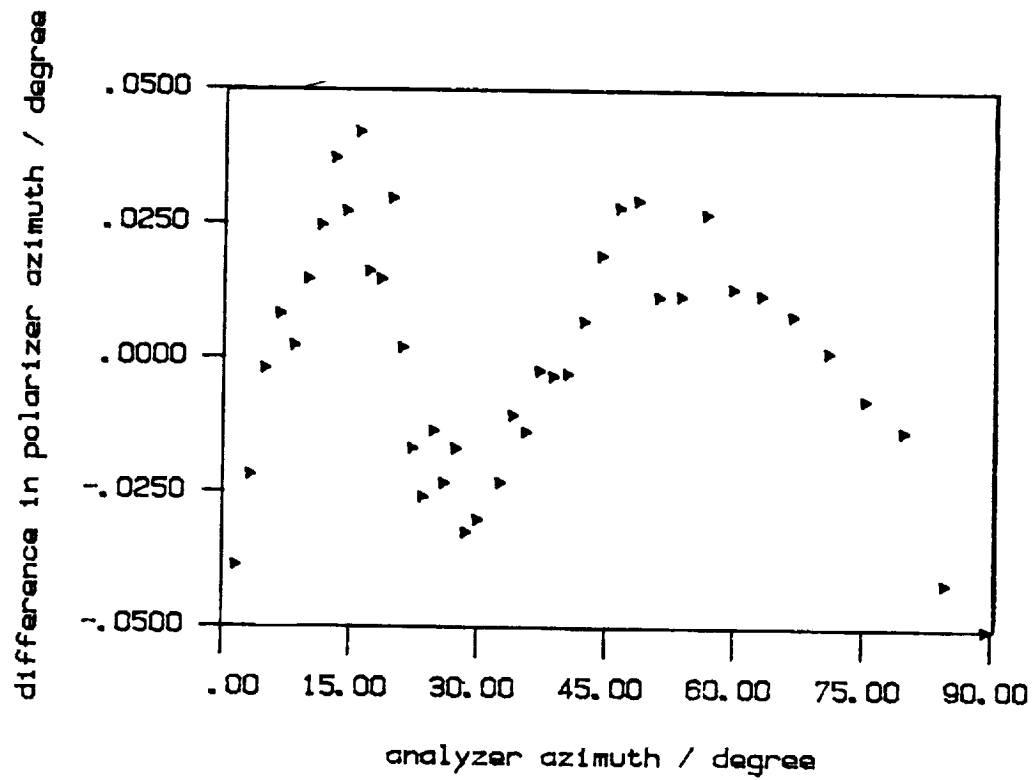


Figure 6.2 Difference Between Measured and Calculated Polarizer Azimuth Versus Analyzer Azimuth for a Carbon Overcoated Computer Disk at an Angle of Incidence of  $57.99^\circ$

The  $\psi$  and  $\Delta$  found with the curve fitting technique described in Appendix E along with the RMS =  $\left( \frac{\sum_{i=1}^n (\beta_c - \beta_m)^2}{n-1} \right)^{1/2}$  (root mean square deviation) and the number of points  $n$  used to find the curve are given in Table 6.1.

We can see that the deviations from the ideal behavior are a few hundredths of a degree. In these curves all the errors (imperfect rotation stages, imperfect polarizers, finite sensitivity of the lock-in amplifier, etc.) will show up. Taking the whole curve helps averaging out the errors and from the calculated RMS, which is smaller or close to the resolution of our rotation stage (.01 degrees), we can conclude that the data follow the theoretical curve very closely.

That the ellipsometric parameters  $\psi$  and  $\Delta$  also coincide with the true  $\psi$  and  $\Delta$ , has to be shown using a standard. It is not easy to get a good standard because surface films on many materials can influence  $\psi$  and  $\Delta$  drastically. Moreover, the optical constants of many materials are not known well enough to allow the comparison between calculated and measured  $\psi$  and  $\Delta$ . We used a silicon substrate with a silicon oxide film ( $\sim 30 \text{ \AA}$ ) on top of it, because the refractive indices for them are very well known and measured  $\psi$  and  $\Delta$  at an angle of incidence of 45 degrees, because we could adjust this angle very accurately using a 90 degree prism, and the change of  $\psi$  with the film thickness at this angle was small  $\left( \frac{\partial \psi}{\partial t} (t=0) = \frac{0.001^\circ}{30 \text{ \AA}} \right)$ . So even a big error in the assumed film thickness would have no influence on the calculations. The change of  $\psi$  with the angle of incidence is  $\frac{\partial \psi}{\partial \alpha} (\alpha=45^\circ) = \frac{0.005^\circ}{0.01^\circ}$ . This means that a precise mounting of the sample is required.



TABLE 6.1

OUTPUT OF THE PD.GO PROGRAM FOR A SILICON WAFER AND  
A CARBON OVERCOATED COMPUTER DISK

Sample	Angle of Incidence $\alpha$	$\psi$	$\Delta$	RMS	n
Silicon oxide on silicon	69.90	10.73	188.25	0.009	67
Carbon overcoated computer disk	57.99	30.52	223.32	0.011	42

TABLE 6.2

REPEATED MEASUREMENTS OF  $\psi$  AND  $\Delta$  OF A CARBON OVERCOATED COMPUTER DISK  
AT AN ANGLE OF INCIDENCE OF  $47.43^\circ$

Run	$\beta_o$	$\alpha_o$	$\psi$	$\Delta$	RMS	No. of Points	Average
1	-.63	1.41	30.536	223.35	0.010	43	$\bar{\psi} = 30.514 \pm 0.019$ $\bar{\Delta} = 223.29 \pm 0.05$
2	-.62	1.35	30.496	223.25	0.009	42	
3	-.59	1.34	30.501	223.25	0.009	42	
4	-.57	1.42	30.524	223.22	0.011	43	

$\beta_o, \alpha_o$  - polarizer and analyzer azimuth offsets

RMS - root mean square deviation between measured and fitted polarizer azimuths

No. - number of points used to fit the curve

Repeated measurements led to an average  $\bar{\psi}$  of  $34.469 \pm 0.045$ . This compares favorably with the theoretically expected 34.477. Using this sample at this angle of incidence the error in  $\Delta$  is too big to serve as a test for the absolute precision. (In practice we would set an angle of incidence such that  $\Delta$  could be determined very accurately too.) But the fact that  $\psi$  is very accurate and that the data follow the theory very closely gives us confidence in our method.

One more test checks the reproducibility of the data (Table 6.2). We have to mention that the precision depends very much on the sample and the angle of incidence. For this reason a suitable angle of incidence should be chosen for all ellipsometric measurement when high accuracy is needed.

$|\cos \Delta|$  lies best between 0.1 and 0.9, because at  $\cos \Delta \approx \pm 1$   $\Delta$  cannot be found very accurately (remember:  $\cos \Delta$  is fitted to the curve) and at  $\cos \Delta = 0$  mode 1 does not work as explained in Chapter 4.

## 6.2 Modes 2 and 3

The next step is to show that  $\psi$  and  $\Delta$  found using Modes 2 and 3 are close to the true  $\psi$  and  $\Delta$  as well.

For this purpose we used a sample with 59 nm silicon oxide film on top of a silicon substrate and measured  $\psi$  and  $\Delta$  at different angles of incidence  $\alpha$  (to cover a large range in  $\psi$  and  $\Delta$ ) using modes 1, 2 and 3. The results are shown in Table 6.3. There are several things to be noted.

1. The offsets  $\alpha_0$  and  $\beta_0$  of the analyzer and polarizer angle (see Appendix E) change with the angle of incidence because the table on which the ellipsometer is mounted is

TABLE 6.3

COMPARISON OF  $\psi$  AND  $\Delta$  OBTAINED BY USING MODES 1, 2 AND 3 FOR A 59 nm THICK SILICON OXIDE FILM ON TOP OF A SILICON SUBSTRATE

$\frac{\alpha}{\text{Deg}}$	Mode 1						Mode 2	Mode 3
	$\frac{\beta_o}{\text{Deg}}$	$\frac{\alpha_o}{\text{Deg}}$	$\frac{\Delta}{\text{Deg}}$	$\frac{\psi}{\text{Deg}}$	$\frac{\text{RMS}}{\text{Deg}}$	No. of Points	$\frac{d\psi}{\text{Deg}}$	$\frac{d\Delta}{\text{Deg}}$
28.09	- .16	.39	188.52	41.506	0.004	30	0.01	- .52
34.36	- .17	.41	193.28	39.613	0.005	28	0.03	- .24
47.43	- .10	.39	206.90	34.537	0.005	29	-0.02	- .52
53.88	- .06	.47	217.90	31.452	0.009	28	0.01	- .36
57.99	- .12	.64	226.95	29.534	0.013	28	0	- .17
63.65	- .05	1.15	243.89	27.393	0.020	27	0	0

$\alpha$  - angle of incidence

$\beta_o, \alpha_o$  - polarizer and analyzer azimuth offsets

RMS - root mean square deviation between measured and fitted polarizer azimuths

No. - number of points used to fit the curve

$d\psi = \psi(\text{mode 1}) - \psi(\text{mode 2})$

$d\Delta = \Delta(\text{mode 1}) - \Delta(\text{mode 3})$

not perfectly flat (no optical table), and the plane of incidence, therefore, moves.

2.  $\psi$  determined with mode 2 taking the offset corrections into account, coincides very well with the  $\psi$  found by the curve-fitting technique (mode 1). The precision in setting  $\beta = 45.00$  influences the precision in  $\psi$ . From  $\frac{\partial \beta}{\partial \alpha}$  ( $\beta = 45^\circ$ ) we can find the error in  $\psi$  caused by an error in setting  $\beta$  equal to 45.00. For most of our samples  $\frac{\partial \beta}{\partial \alpha} > 1$  and, therefore, the error in  $\psi$  is smaller than the error in setting  $\beta = 45.00$ .

3. For mode 3 the quarter-wave plate had to be inserted. The azimuth was adjusted such that modes 1 and 3 gave the same  $\Delta$  at an angle of incidence of 63.65. It can be seen that the error in  $\Delta$  is somewhat larger than the error in  $\psi$ . This is usually the case in ellipsometry, especially in our mode of operation, where we introduced an additional optical element. This will introduce new errors, even though we set the analyzer angle equal to  $\psi$  to minimize the effect of imperfections of the quarter-wave plate (see Chapter 5).

Because we did not change the azimuth  $\tau$  of the quarter-wave plate when changing the angle of incidence  $\tau$  is not always exactly equal to 45.00. This error could be eliminated or at least reduced by using an optical table. This problem is not encountered at all when scanning across a surface.

We have to mention that mode 3 as described above determines  $\Delta$  not completely independent of  $\psi$ , because  $\alpha$  is set equal to  $\psi$ . With an ideal quarter-wave plate it would not be necessary to set  $\alpha = \psi$  as shown in Chapter 5.

## CHAPTER 7

### SOME APPLICATIONS

In this chapter we will show some applications of our ellipsometer and demonstrate the usefulness of the different modes of operation.

In Section 7.1 we show  $\psi$  and  $\Delta$  scans across a wear track. From these scans we could get some clues about the kind of material formed and the amount of it.

In Section 7.2 we performed multiple angle of incidence measurements to calculate the thickness of a carbon overcoat on a computer disk. Very high precision is necessary to determine more than just one unknown of a sample.

In Section 7.3 we discuss the importance of selecting an appropriate angle of incidence to measure the thickness of a silicon oxide on top of a silicon substrate with high precision.

#### 7.1 Analysis of Wear Tracks

In this section we will summarize an ellipsometric analysis of a wear track produced by rotating a steel ball against a steel plate. The objective of the investigation was to determine the nature and amount of oxide formed under elastohydrodynamic lubrication with different oils and additives present. A more detailed description can be found in a paper by Lauer, Marxer and Jones [26].

The first step in the analysis was to find the optical constants of the steel plate. We found from  $\psi$  and  $\Delta$  measured at

several angles of incidence that the steel could be well represented by a single complex refractive index  $\hat{n}$  ,

$$\hat{n}_s = 2.14 + i \ 3.29 \quad (7.1)$$

I do not discuss the production of the wear track here. We assumed that a single film had been formed in the process. From scans through the wear track we determined average  $\bar{\psi}$  and  $\bar{\Delta}$  inside the wear track for two angles of incidence.

For our one-film model only a 6 nm thick film with a refractive index

$$\hat{n}_F = 2.42 + i \ 1.72 \quad (7.2)$$

agreed with the data. This refractive index does not agree with the one for  $\text{Fe}_2\text{O}_3$ , nor with the one for  $\text{Fe}_3\text{O}_4$  (taken from Leberknight and Lustman [33]). But both the real refractive index and the extinction coefficient were in good agreement with a model assuming that the film consists of a mixture of the bulk material and of  $\text{Fe}_3\text{O}_4$ . This is in agreement with the finding of Sakurai who also showed the presence of  $\text{Fe}_3\text{O}_4$  (and no  $\text{Fe}_2\text{O}_3$ ) using electron spectroscopy (private communication with Professor Lauer). For this mixture we assumed a refractive index to follow Eq.(7.3)

$$\hat{n}_F = x \cdot \hat{n}_o + (1 - x) \hat{n}_s \quad (7.3)$$

where  $\hat{n}_s$ ,  $\hat{n}_o$  are the refractive indices of the steel and  $\text{Fe}_3\text{O}_4$  oxide respectively, and  $x$  is the relative amount (mole fraction) of oxide present. Here  $x$  was found to be approximately .55.

A constant film thickness inside the wear track would give a constant  $\psi$  and  $\Delta$  when scanning across the surface. But we can see that  $\psi$  and  $\Delta$  inside the wear track vary a lot (Figures 7.1 and 7.2). That means that the film thickness and maybe even the material composition is not homogeneous. In Figures 7.3 and 7.4 theoretical  $\psi$  and  $\Delta$  versus film thickness curves with the relative amount of oxide  $x$  being a parameter are shown. The excursions seen in Figures 7.1 and 7.2 can be explained qualitatively postulating that the film is present in a patchy way. Visual inspection under an optical microscope and Auger electron spectroscopy support this view.

## 7.2 Thickness Measurement for a Carbon Overcoating on a Computer Disk

This section summarizes a part of the paper by Lauer and Marxer [27] on carbon overcoated and lubricated computer disks. The objective of the investigation was to determine whether it is possible to measure the thickness of a carbon overcoat on top of a computer disk, which by itself consists of several metallic layers (see Figure 7.5).

We received two disks where all the layers were present and some disks, where one or more of the metallic layers were not put on. This should have allowed to determine all the optical constants and film thicknesses for the different layers. But the analysis of the data showed (see below) that it was sufficient to analyze the disk with all the layers present and the disk which had all the layers except the top one.



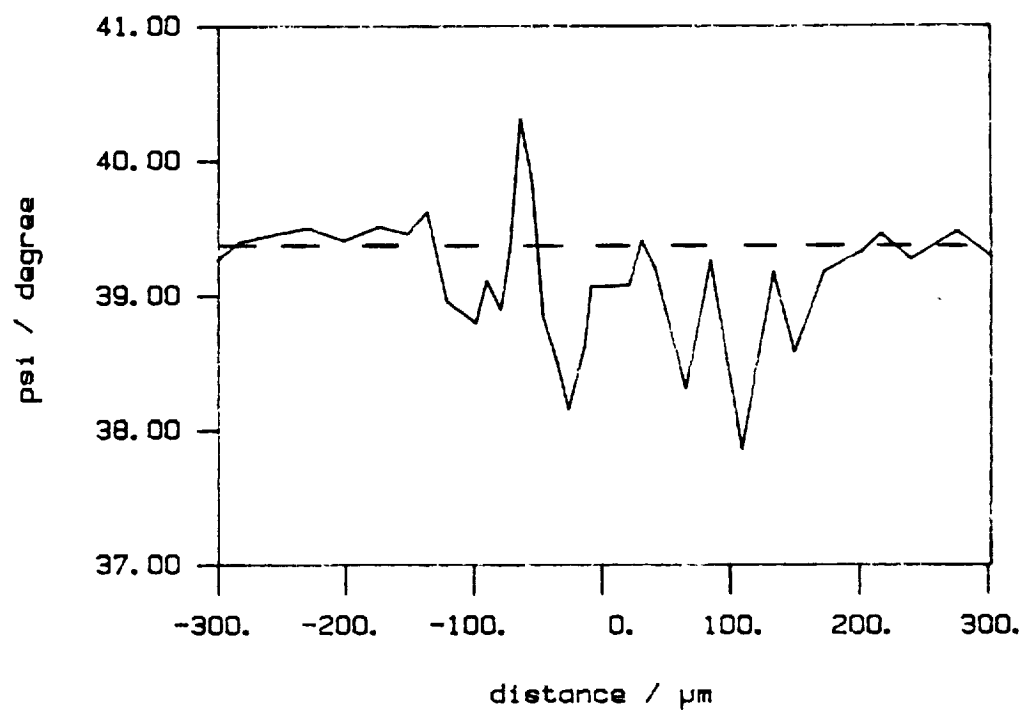


Figure 7.1 Variation of  $\psi$  Over a Wear Track Run on TCP for an Angle of Incidence of  $45.7^\circ$ . The broken line corresponds to the Value in the Absence of an Oxide Coating

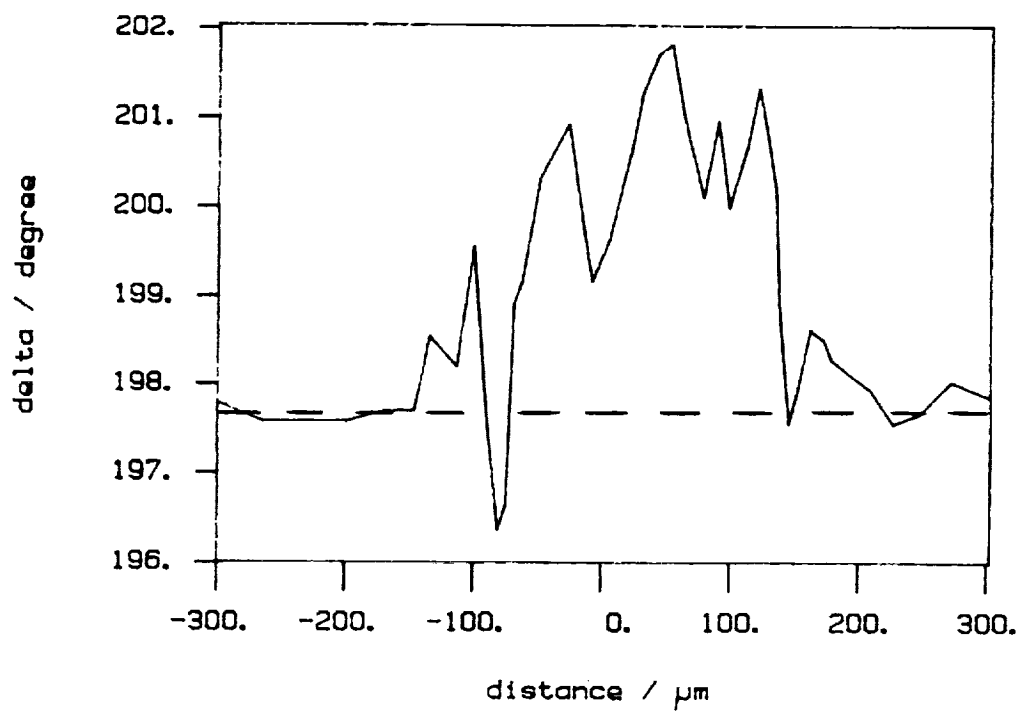


Figure 7.2 Variation of  $\Delta$  Over a Wear Track Run on TCP for an Angle of Incidence of  $45.7^\circ$ . The broken line corresponds to the Value in the Absence of an Oxide Coating.

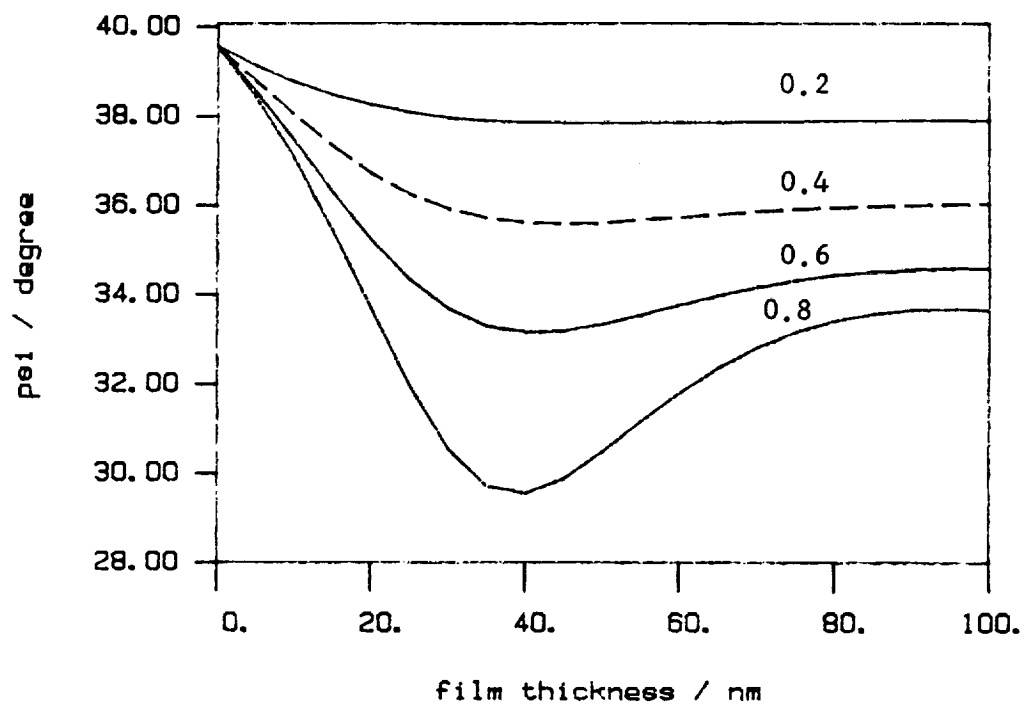


Figure 7.3  $\psi$  vs Film Thickness Calculated for Films Containing Different Amounts (Mole Fraction) of  $\text{Fe}_3\text{O}_4$  on Top of a Surface with Complex Refractive Index  $\hat{n}_s = 2.14 + i3.29$

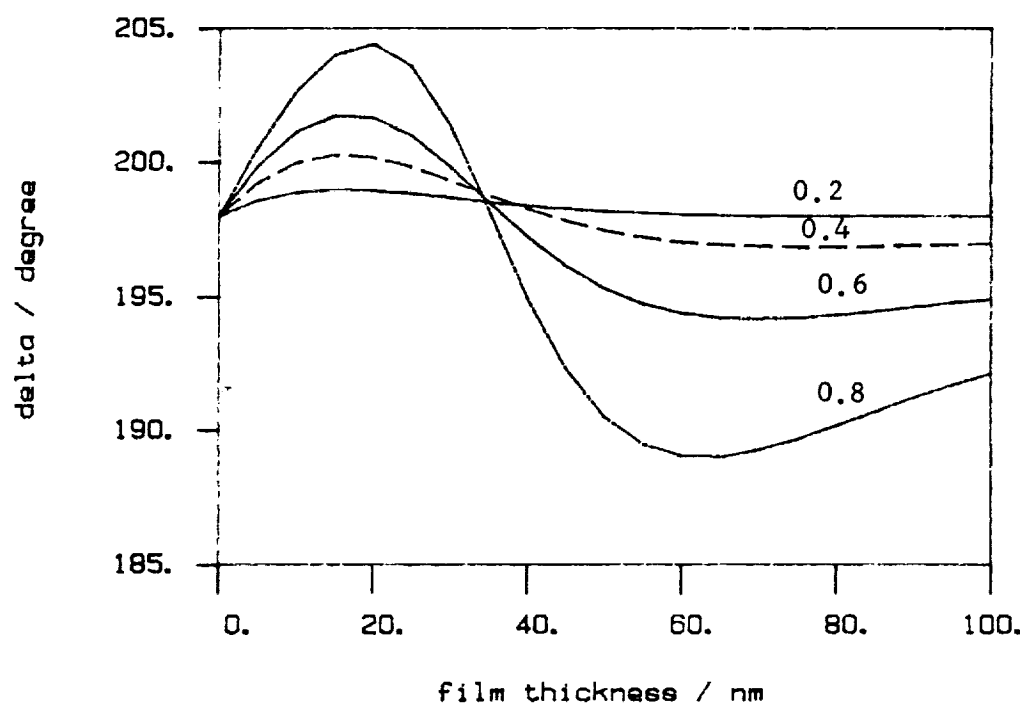


Figure 7.4  $\Delta$  vs Film Thickness Calculated for Films Containing Different Amounts (Mole Fraction) of  $\text{Fe}_3\text{O}_4$  on Top of a Surface with Complex Refractive Index  $\hat{n}_s = 2.14 + i3.29$

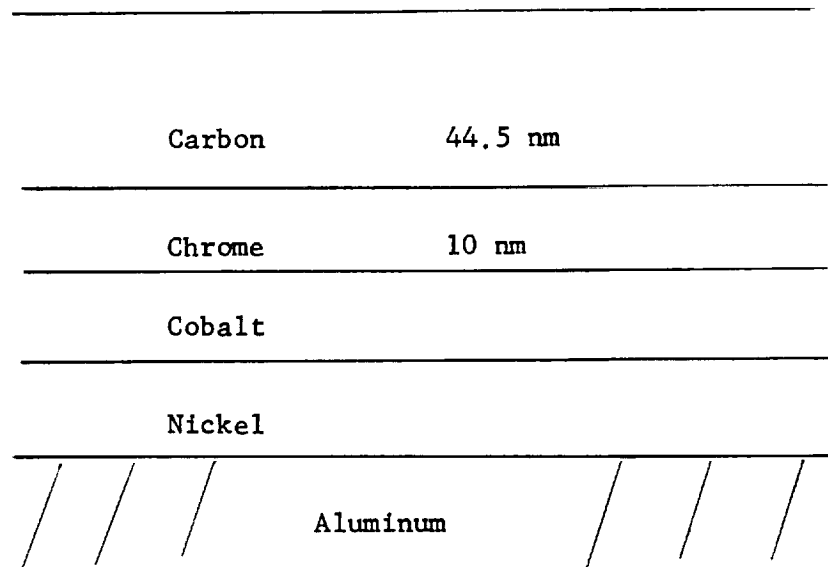


Figure 7.5 Schematic of the Top Layers of a Computer Disk

$\psi$  and  $\Delta$  were determined at many angles of incidence  $\alpha_i$  for the two disks (Figures 7.6 and 7.7) using modes 1 and 2 as explained in Chapter 3. As an example we show Figures 7.8 and 7.9 where a curve was fitted to the experimentally found (polarizer, analyzer) pairs at two angles of incidence for the two disks, respectively, the fitted curve determining  $\psi$  and  $\Delta$ .

We tried to reproduce the experimentally found  $\psi(\alpha_i)$  and  $\Delta(\alpha_i)$  points for the nonovercoated disk using both a model where the sample consisted of a bare substrate and a model where we had a film on top of a substrate. A least square fit to the experimental data points was performed using the subroutine SEARCH of the program elli.go (see Appendix E) and the result of the calculation is summarized in Table 7.1. We can see from this table (see RMS) and from Figure 7.6 that the simpler bare substrate model is as good as the one-film model.

Similar calculations were performed for the carbon overcoated disk. Table 7.2 contains a summary of the results.

The bare substrate model could be readily excluded, because we knew that the carbon thickness is smaller than 100 nm. With the refractive index we got for the film we would see the carbon/chrome interface in contradiction to the assumption of a bare substrate model.

For both one-film models we used the refractive index found for the nonovercoated disk as substrate index. As can be seen in the table the one-film model where we fitted the film refractive index and the film thickness gave a low RMS, but the refractive index was unreasonable. Using the literature value (McCartney and Ergun [34])

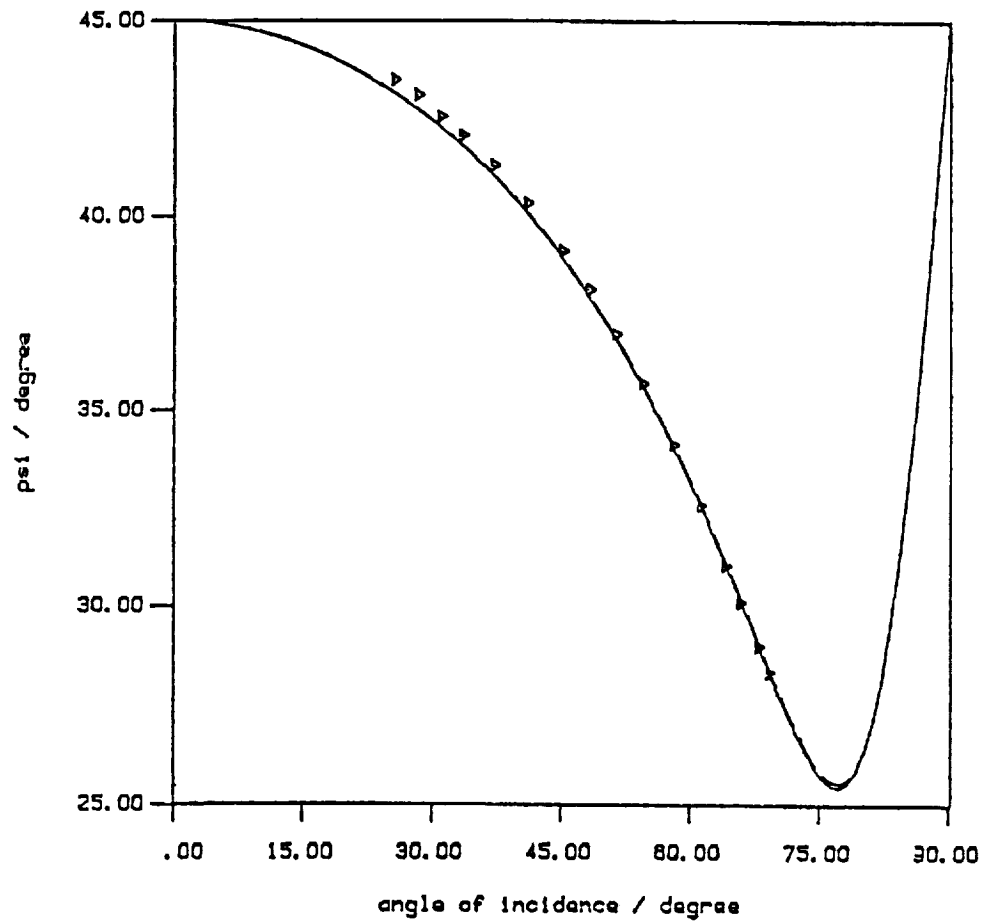


Figure 7.6a  $\psi$  vs Angle of Incidence for the Nonovercoated Disk. The solid line represents the best fit to the triangular data points with a bare substrate model and the broken line the best fit with a single film model. The two lines almost coincide.

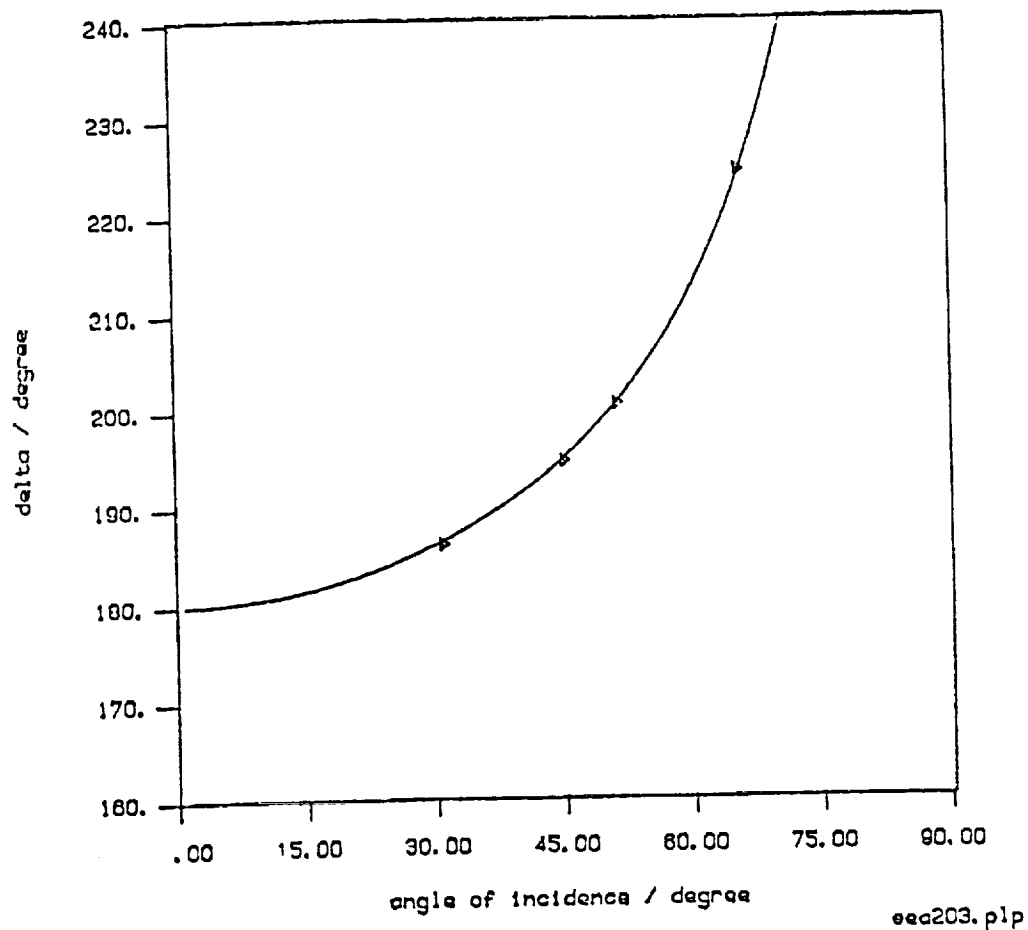


Figure 7.6b  $\Delta$  vs Angle of Incidence for Nonovercoated Disk. The two curves, which represent the best fits to the triangular data points for the "bare substrate model" and the "one film model", respectively, coincide in this figure.



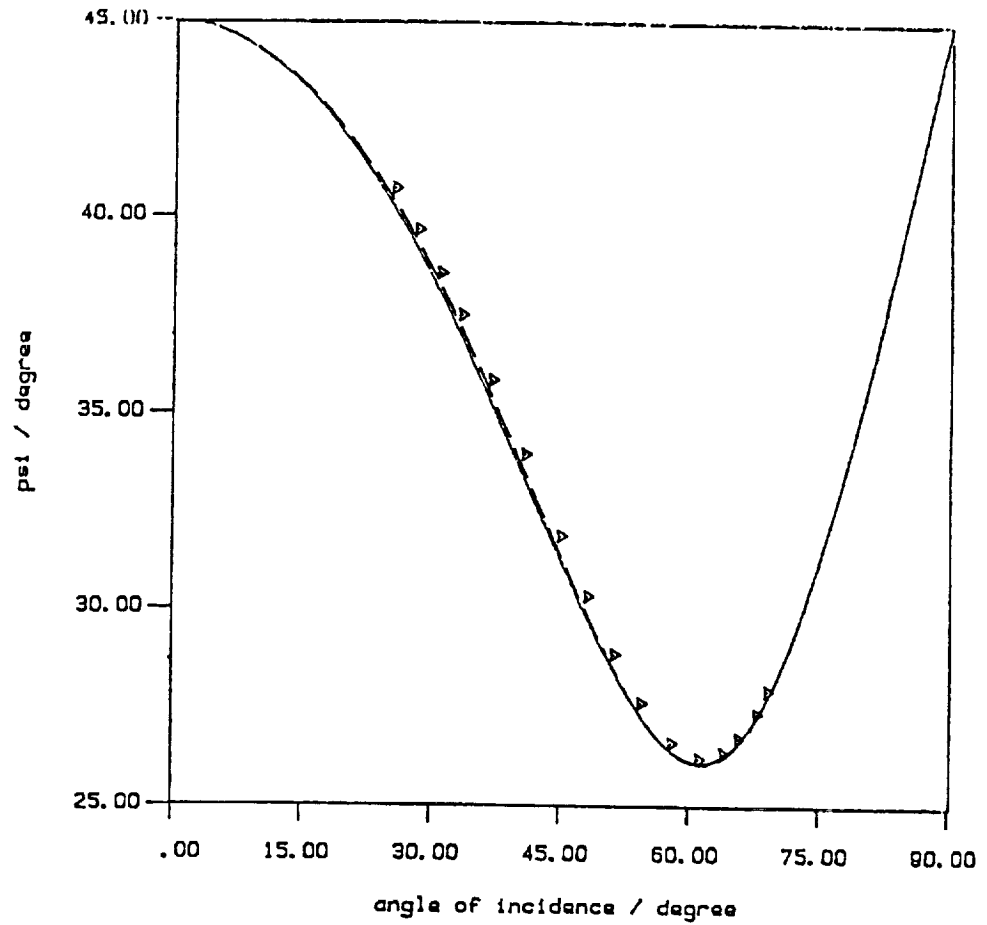


Figure 7.7a  $\psi$  vs Angle of Incidence for the Carbon Overcoated Disk. The solid line represents the best fit to the triangular data points with a bare substrate model and the broken line the best fit with a single film model.

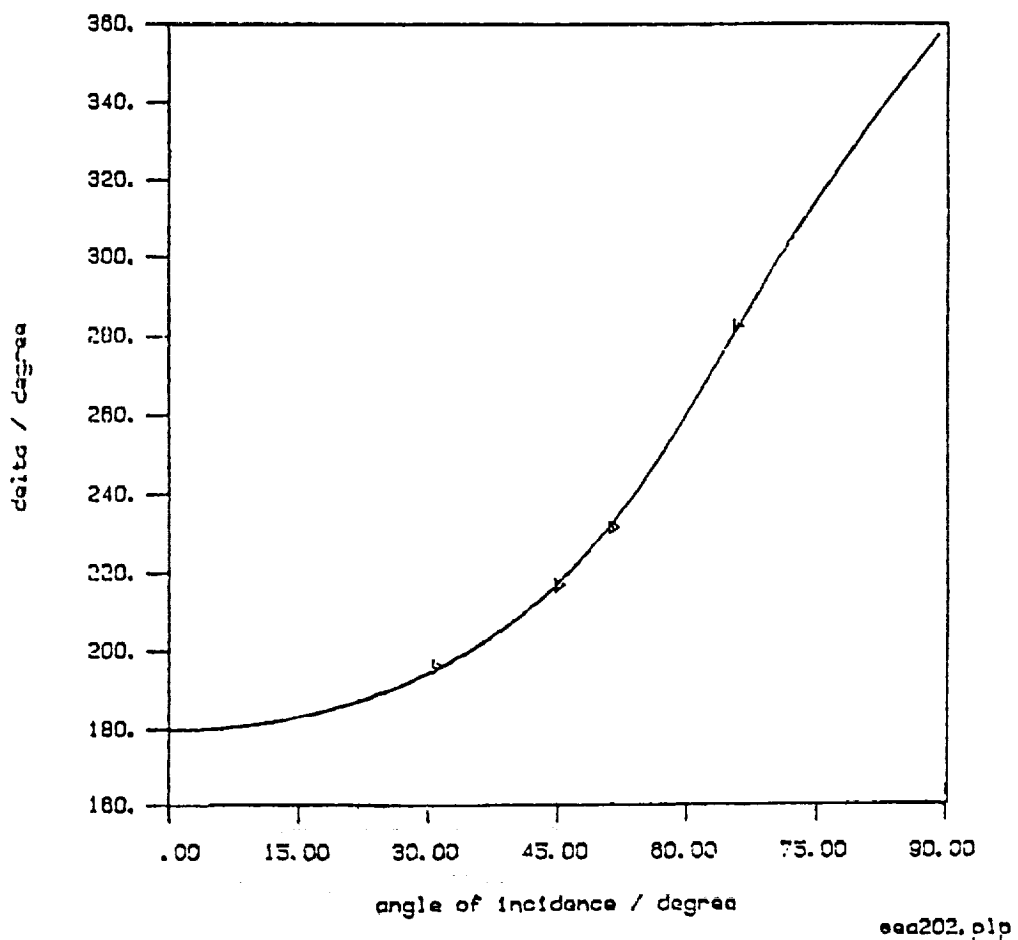


Figure 7.7b  $\Delta$  vs Angle of Incidence for the Carbon Overcoated Disk. The two curves, which represent the best fits to the triangular data points for the "bare substrate model" and the "one film model", respectively, coincide in this figure.

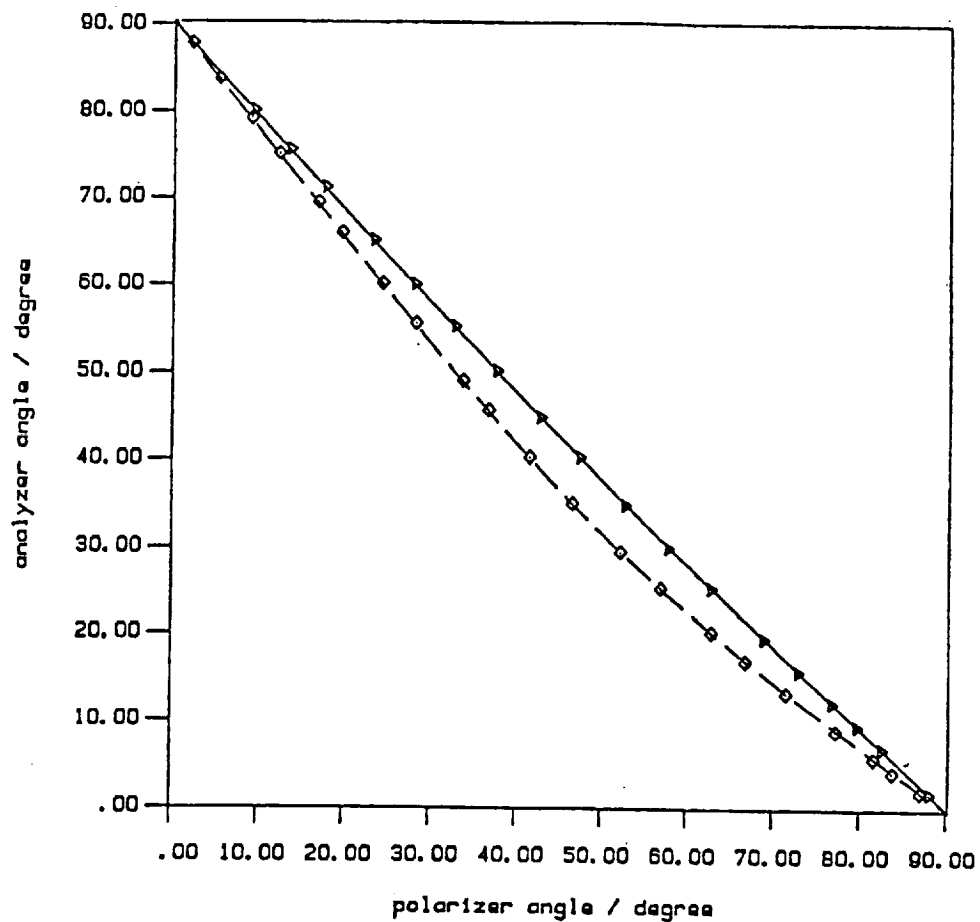


Figure 7.8 Analyzer-Polarizer Angle Data for a Nonovercoated Disk at Angles of Incidence of  $30.86^\circ$  and  $51.27^\circ$ . The continuous curves represent the fit to Eq.(3.7), the solid one for  $30.86^\circ$  and the broken one for  $51.27^\circ$ .

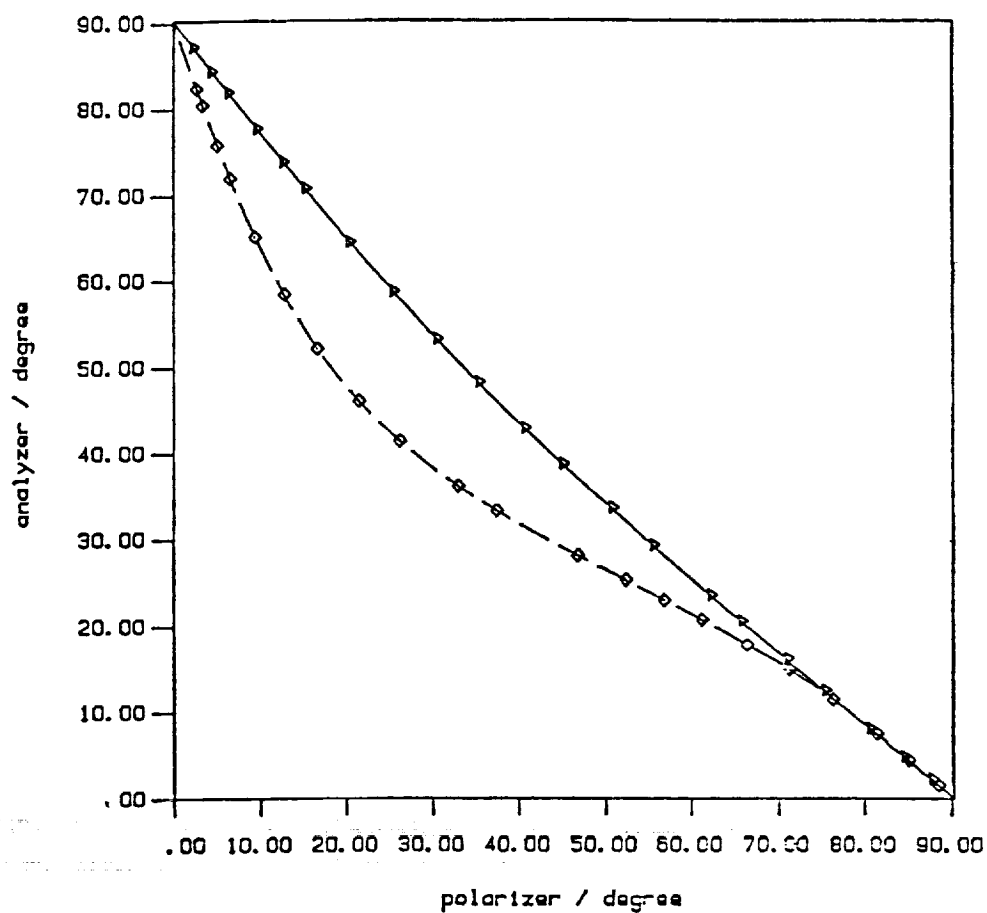


Figure 7.9 Analyzer-Polarizer Angle Data for the Carbon Overcoated Disk at Angles of Incidence of  $30.86^\circ$  and  $51.27^\circ$ . The continuous curves represent the fit to Eq.(3.7), the solid one for  $30.86^\circ$  and the broken one for  $51.27^\circ$ .

TABLE 7.1

INPUT AND OUTPUT OF THE PROGRAM SEARCH, WHICH PERFORMED A LEAST  
 SQUARE FIT FOR THE EXPERIMENTALLY DETERMINED  $\psi_i$  AND  $\Delta_i$  AT  
 ANGLES OF INCIDENCE  $\alpha_i$  FOR BOTH A BARE SUBSTRATE  
 AND A ONE-FILM MODEL  
 Nonovercoated Disk

Model	Input	Output
Bare Substrate	$(\alpha_i \ \psi_i \ \Delta_i)$	$\hat{n}_s = 2.73 + i \ 3.18; \ \text{RMS} = 0.22^\circ$
One Film	$(\alpha_i \ \psi_i \ \Delta_i)$	$\hat{n}_s = 1.45 + i \ 1.25$ $\hat{n}_F = 3.5 + i \ 3.5 \quad \text{RMS} = 0.22^\circ$ $t_F = 5 \text{ nm}$

TABLE 7.2

INPUT AND OUTPUT OF THE SEARCH PROGRAM, WHICH PERFORMED A LEAST  
 SQUARE FIT TO THE DATA POINTS  $\psi_i$ ,  $\Delta_i$  AT SEVERAL ANGLES  
 OF INCIDENCE  $\alpha_i$  FOR DIFFERENT MODELS  
 (Carbon Overcoated Disk)

	Input	Output
Bare substrate	$(\alpha_i \ \psi_i \ \Delta_i)$	$\hat{n}_s = 1.20 + i \ 1.18$ RMS = $0.55^\circ$
One film model	$(\alpha_i \ \psi_i \ \Delta_i)$ $\hat{n}_s = 2.73 + i \ 3.18$	$\hat{n}_F = 1.03 + i \ 0.521$ RMS = $0.37^\circ$ $t_F = 62.5 \text{ nm}$
One film model	$(\alpha_i \ \psi_i \ \Delta_i)$ $\hat{n}_s = 2.73 + i \ 3.18$ $n_F = 2.05$	$k_F = 0.70$ RMS = $0.53^\circ$ $t_F = 44.5 \text{ nm}$

for only the real refractive index ( $n = 2.05$ ), because the extinction coefficient depends on the crystal orientation (see Table 7.3), gave an extinction coefficient of 0.70, which is an average between the extinction coefficients in the direction parallel and perpendicular to the optical axis, and a film thickness of 44.5 nm in good agreement with weight measurements. The extinction coefficient indicates that the crystals are oriented in a random way.

Because we now know the optical constants of the substrate and the film, we can make plots of  $\psi$  and  $\Delta$  versus film thickness. Then using this curve a simple  $\psi$  measurement (for example) will give us the carbon film thickness.

This investigation shows that not too many unknowns can be determined for one sample even though  $\psi$  and  $\Delta$  were determined at many different angles of incidence. But once the refractive indices are known, the determination of the film thickness would cause no problems, because  $\psi$  and  $\Delta$  change very much with film thickness.

### 7.3 Silicon Oxide ( $\text{SiO}_2$ ) Film Thickness Measurement

To measure the thickness of silicon oxide on top of a silicon substrate did not cause any problems, because the optical constants of silicon and silicon oxide are well known and only the film thickness had to be determined. But this description should serve as an example of how important it is to select an appropriate angle of incidence.

Theoretical  $\psi$  and  $\Delta$  versus film thickness curves were calculated (see Figures 7.10 and 7.11) using the refractive indices for silicon and silicon oxide given in Table 7.4 in order to find the

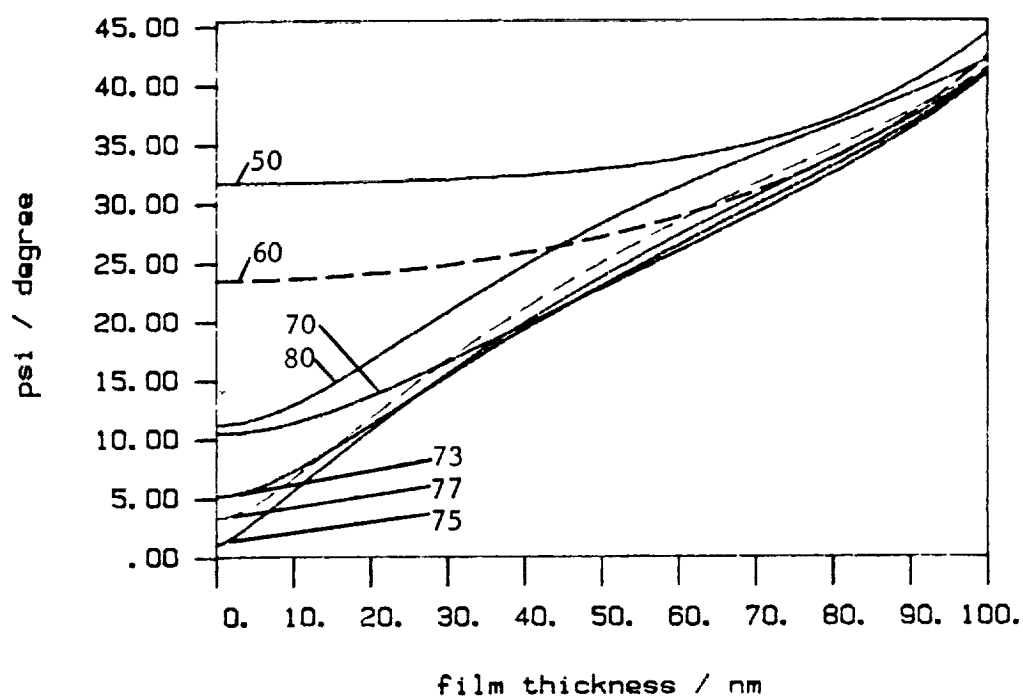


Figure 7.10 Calculated  $\psi$  vs Film Thickness of Silicon Oxide on a Silicon Substrate for Various Angles of Incidence



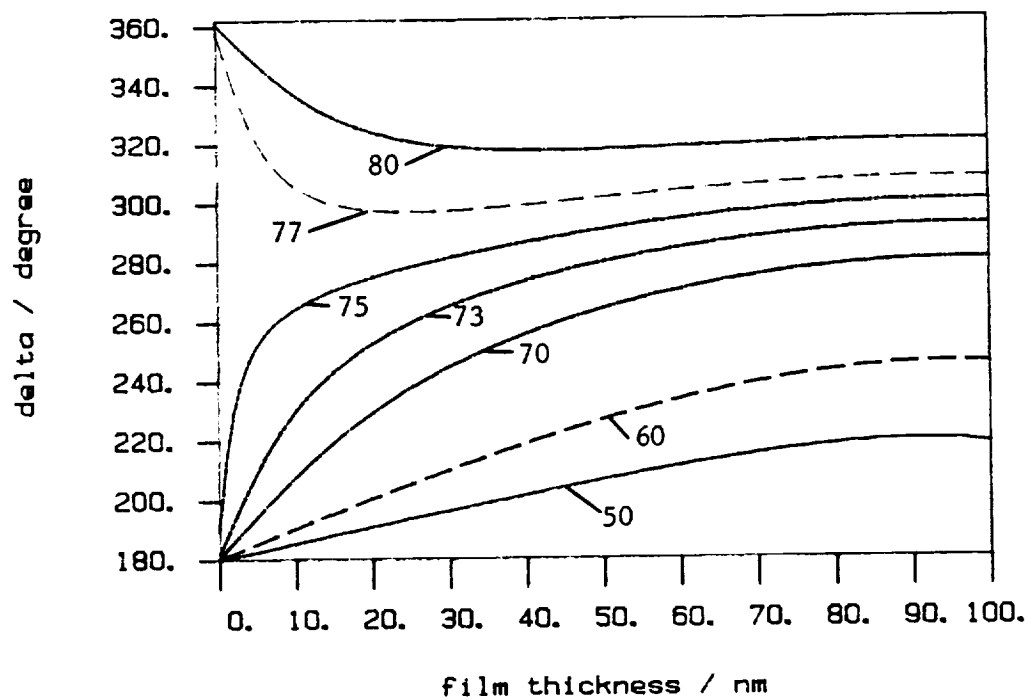


Figure 7.11  $\Delta$  vs Film Thickness of Silicon Oxide on a Silicon Substrate for Various Angles of Incidence

TABLE 7.3  
REFRACTIVE INDEX OF GRAPHITE PARALLEL ( $\hat{n}_{||}$ ) AND  
PERPENDICULAR TO THE OPTICAL AXIS ( $\hat{n}_{\perp}$ )

$$\hat{n}_{||} = 2.04 + i \ 0.02$$

$$\hat{n}_{\perp} = 2.15 + i \ 1.42$$

at  $\lambda = 550 \text{ nm}$

TABLE 7.4  
REFRACTIVE INDICES FOR SILICON AND SILICON OXIDE  
TAKEN FROM PEDINOFF AND STAFSUDD [35]

Silicon             $n = 3.8714 + i \ 0.025$

Silicon oxide     $n = 1.45$

at  $\lambda = 632.8 \text{ nm}$

angle of incidence for which highly accurate measurements were to be expected (i.e., large change of  $\psi$  or  $\Delta$  with film thickness).

Because we knew that the oxide thickness was approximately 3 nm (from ESCA measurements), we could concentrate on the  $\psi$  and  $\Delta$  behavior for very thin films. We see from Figure 7.10 that  $\psi$  varies only slightly with film thickness. Taking into account that the determination of the angle of incidence involves a small error we concluded that we could not use  $\psi$  to find the film thickness.

For  $\Delta$  the situation is different. As can be seen in Figure 7.11 the change of  $\Delta$  with film thickness is very big for angles between 70 and 80 degrees. But we have to remember that  $\Delta$  cannot be determined very accurately (using mode 1) close to 180, 270 and 360 degrees which excludes angles between 75 and 77 degrees.

We selected an angle of incidence of 69.90 degrees and from the measured deltas the film thickness could be determined (see Table 7.5). The error in the film thickness is approximately 0.1 nm.

TABLE 7.5

FILM THICKNESS DETERMINED FOR FIVE "SILICON OXIDE  
ON SILICON SUBSTRATE" SAMPLES

Sample Number	Delta/Degrees	Film Thickness/nm
1	189.3	3.0
2	188.7	2.75
3	189.9	3.2
4	189.4	3.0
5	188.4	2.65

## CHAPTER 8

### DISCUSSION AND CONCLUSIONS

#### 8.1 Ellipsometry

As we have seen in the foregoing discussion, ellipsometry is an extremely sensitive tool for the analysis of surfaces. The two ellipsometric parameters  $\psi$  and  $\Delta$ , which are measured for a particular sample at one angle of incidence, can be determined with very high precision. The more difficult step is getting useful information (film thickness, optical constants) from the measured quantities, because the success of a calculation depends very much on the use of a good model for the surface (e.g., one film model).

In this work the surface is characterized by a planar multilayer structure, and the refractive index of each layer is assumed to be isotropic. This is commonly done in ellipsometry and the theory has been worked out a long time ago (Drude [4]). But only recently, with the availability of computers, multilayer structures can be analyzed in a reasonable amount of time.

The novelty in this thesis is the construction of an instrument with some unique features. To our knowledge there are only two instruments described in the literature (Monin and Boutry [14], Sullo and Moore [24]), which are based on the same principle (see "Faraday Modulated Ellipsometry" in Chapter 1) as our instrument. We needed both high absolute precision for a multiple angle of incidence analysis and high speed for scans (to collect some thousand data points in a short time). To do that we adapted the good features of the two designs and developed some new ones, which are described below.

1. We take many (30 - 40) (analyzer, polarizer)-pairs to calculate  $\psi$  and  $\Delta$  more accurately.
2. No calibration prior to an experiment is necessary.
3. A mode was developed which gives  $\psi$  independently of  $\Delta$ .
4. A mode was developed which gives  $\Delta$  independently of  $\psi$ .
5. A resolution of 20  $\mu\text{m}$  was obtained without any lenses between the polarizer and the analyzer.

Because the error in the angle of incidence is a few 0.01 degrees and this error should not be larger than the error in  $\psi$  and  $\Delta$ , it would be necessary to improve both the sample alignment and the resolution of the rotation stages to obtain even higher precision. We did not have the funding to do that, but our method has the potential of competing with the dynamic photometric ellipsometers (see Chapter 1) for highest precision. Because in our design we determine a null, the nonlinearity of the detector is of no importance, in contrast to photometric ellipsometers.

The modes, where  $\psi$  or  $\Delta$  can be determined independently of each other, were extremely useful for scans through wear tracks.

Because the  $\Delta$ -scan uses a quarter-wave plate, which usually introduces the largest error in an ellipsometric measurement, it was necessary to devise means to reduce the influence of its nonideal behavior. The  $\psi$ - and  $\Delta$ -scans developed here could not be performed with photometric and angle tuning ellipsometers (see Chapter 1). An important application is a  $\psi$ -scan of a dielectric, because  $\Delta$  is known (180 or 360 degrees) and  $\psi$  characterizes the sample completely. The accuracy of 0.01 degree in the azimuth of our rotation stages corresponds to a

resolution of 0.0005 in the refractive index of a dielectric with  $n = 1.5$  at an angle of incidence of 45 degrees. This means that a  $\psi$  versus position curve (e.g., gradient index fiber) or a  $\psi$  versus wavelength curve (e.g., dispersion analysis) would show very small changes of  $n$ . A dispersion analysis is easily done, because no quarter-wave plate is used in a  $\psi$ -scan.

Our design is also superior to the angle tuning ellipsometer in another aspect. We can measure  $\psi$  and  $\Delta$  at several angles of incidence, whereas the angle tuning ellipsometer works usually only at one angle of incidence. An additional advantage of our method is the ease of operation, if we need high precision only in relative changes. We first set the angle of incidence where large changes of the ellipsometric parameters are to be expected. Then we set the polarizer at an azimuth of 45 degrees and mount the sample. The analyzer in the feedback loop locks in at an azimuth  $\alpha$ , which gives  $\psi$  without calculations ( $\psi = \alpha$ ). We then turn a switch to replace the analyzer in the feedback loop by the polarizer, swing the quarter-wave plate into the optical path, and the polarizer locks in at an azimuth  $\beta$ , which gives  $\Delta$  with a very simple calculation ( $\Delta = 2\beta + 90$ ). No computer or even a pocket calculator is necessary to determine  $\psi$  and  $\Delta$ .

The arrangement of all the optical components was chosen so that we obtained a resolution of 20  $\mu\text{m}$  with no lenses between the laser and analyzer. The set-up was optimized using ray tracing calculations. Usually the whole laser beam is used in ellipsometry, and

the resolution is given by the beam diameter. Some ellipsometers focus the light onto the sample; this means that the light is incident at a whole range of angles of incidence. Moreover, stress induced birefringence of the lenses will influence the measurement. With our instrument, we do not have these problems.

The only disadvantage of our ellipsometer is the fact that it is not very fast (i.e., it cannot see changes occurring on a ms-timescale), because (i) the lock-in amplifier has a finite time constant (1.25 ms), (ii) an increase in speed requires a higher fundamental frequency, which leads to a decrease of the modulation amplitude (coil impedance), and (iii) the stages are rotated mechanically. Therefore, to study fast surface reactions, a photometric ellipsometer should be chosen.

The slow speed of our instrument was not a serious drawback in our measurements, because we did not study surface reactions. But the other features, which were developed for a Faraday-modulated ellipsometer for the first time, were instrumental in the analysis of our samples. Without them, the experiments described in this work could not have been performed.

## 8.2 Summary of the Experiments

The original purpose for building this ellipsometer was the analysis of wear tracks and computer disks. In the following I summarize briefly what we learned from our investigations.



### 8.2.1 Wear Track Analysis

The steel plate, which contains iron, carbon, chrome, vanadium and molybdenum, could be represented by an effective index of refraction.  $\psi$ - and  $\Delta$ -scans through the wear tracks at different angles of incidence showed that the oxide was present in a patchy way. Furthermore, the oxide could be identified as  $\text{Fe}_3\text{O}_4$ . The average thickness of the patches and the presence of  $\text{Fe}_3\text{O}_4$  were in agreement with an analysis by Auger electron spectroscopy and electron spectroscopy.

It was found that certain additives, which were more likely to lead to scuffing failure, produced patches of nearly oxide-free surfaces in wear tracks. Since oxide-free surfaces are more likely to weld than others, their greater tendency to scuffing can be explained.

### 8.2.2 Carbon Coating

The computer disk without the carbon overcoat has a very thin chrome layer on top. It is likely that the chrome film thickness is not uniform and, in addition, is covered by an oxide film. Nevertheless, an analysis showed that this disk could be well represented by one effective index of refraction.

The complex refractive index for graphite is different parallel ( $\hat{n}_{||}$ ) and perpendicular ( $\hat{n}_{\perp}$ ) to the optical axis. But because the real refractive index is approximately the same in both directions, only the extinction coefficient and the thickness of the graphite layer had to be determined. The resulting thickness (44.5 nm) and extinction coefficient (0.70) were, considering the many approximations made, close

to the thickness found with weight measurement (40 nm) and an average extinction coefficient of 0.68 given in the literature (Senftleben and Benedict [36] for green light), from which we deduced that the graphite crystals were randomly oriented. An analysis where the carbon film was characterized by 32 films and the refractive index was given alternately by  $\hat{n}_{||}$  and  $\hat{n}_{\perp}$ , reproduced the data even better (not shown). But it is clear that the thin film theory used in this work is not applicable for crystals with an anisotropic refractive index.

The goal of the investigation was to measure the thickness of the carbon overcoat. Now we can do this very easily. We calculate a curve of  $\psi$  or  $\Delta$  versus carbon-film thickness, and then a measurement of  $\psi$  or  $\Delta$  at one angle of incidence gives the thickness very quickly with the help of this curve.

### 8.2.3 Silicon Oxide Film

By using literature values for the optical constants of silicon and silicon oxide, and by representing the surface by a simple "one film on a substrate" model, the film thickness can be determined with high accuracy. This measurement is routinely done in industry with hardware and software dedicated to this particular sample.

### 8.3 Summary

The experiments performed with our instrument, which was built for the analysis of samples encountered in a tribology lab, could not be done with a commercially available ellipsometer or even a research ellipsometer as described in the literature. Our instrument

has the potential for very high absolute precision, is extremely sensitive for relative changes using the scanning modes, and allows one to find the ellipsometric parameters very quickly without the use of a calculator. These features make the instrument very versatile and useful in different kinds of applications, e.g., quality control in an industry environment, quick film thickness measurement in a tribology lab, or multiple angle of incidence analysis for a complete characterization of a surface.

# LITERATURE CITED

1. J.L. Lauer, S.S. Fung and W.R. Jones, Jr., "Topological Reaction Rate Measurements Related to Scuffing," ASLE Trans., 27, 288 (1984).
2. J.L. Lauer, N. Marxer and W.R. Jones, Jr., "Optical and Other Property Changes of M-50 Bearing Steel Surfaces for Different Lubricants and Additives Prior to Scuffing," ASLE Trans., 29, 13 (1986).
3. Lord Rayleigh, Phil. Mag., 33, 1 (1980).
4. P. Drude, Ann. Physik Chemie, 39, 481 (1890).
5. P. Drude, Ann. Physik Chemie, 36, 532, 865 (1889).
6. R.J. King and M.J. Downs, "Ellipsometry Applied to Films on Dielectric Substrates," Surface Science, 16, 288 (1969).
7. J.C. Charmet and P.G. deGennes, "Ellipsometric Formulas for and Inhomogeneous Layer with Arbitrary Refractive-Index Profile," J. Opt. Soc. Am., 73, 1777 (1983).
8. T. Smith, "Effect of Surface Roughness on Ellipsometry of Aluminum," Surface Science, 56, 252 (1976).
9. J.R. Blanco, P.J. McMarr and K. Vedam, "Roughness Measurements by Spectroscopic Ellipsometry," Appl. Opt., 24, 3773 (1985).
10. T.V. Vorburger and K.C. Ludema, "Ellipsometry of Rough Surfaces," Appl. Opt., 19, 561 (1980).
11. R.M.A. Azzam and N.M. Bashara, Ellipsometry and Polarized Light, North Holland, New York, 1977.
12. U. Merkt, "Precision of Ellipsometer Nulling," Appl. Opt., 20, 307 (1981).
13. A.B. Winterbottom, "Increased Scope of Ellipsometric Studies of Surface Film Formation," in "Ellipsometry in Measurement of Surfaces and Thin Films," Washington, 1963.
14. J. Monin and G.A. Boutry, "Conception, Realisation et Fonctionnement d'un Nouvel Ellipsometre," Nouv. Rev. Optique, 4, 159 (1973).
15. H.M. O'Bryan, "The Optical Constants of Several Metals in Vacuum," J. Opt. Soc. Am., 26, 122 (1936).

16. A.B. Marchant and J.J. Wrobel, "Simple Ellipsometer Design," Appl. Opt., 20, 2040 (1981).
17. A. Moritani, Y. Okuda, H. Kubo and J. Nakai, "High-Speed Retardation Modulation Ellipsometer," Appl. Opt., 22, 2429 (1983).
18. A. Roeseler, "Spectroscopic Ellipsometry in the Infrared," Infrared Physics, 21, 349 (1981).
19. G.E. Jellison, Jr. and D.H. Lowndes, "Time-Resolved Ellipsometry," Appl. Opt., 24, 2948 (1985).
20. D.E. Aspnes and P.S. Hauge, "Rotating-Compensator/Analyzer Fixed-Analyzer Ellipsometer: Analysis and Comparison to Other Automatic Ellipsometers," J. Opt. Soc. Am., 66, 949 (1976).
21. D. Chandler-Horowitz and G.A. Candela, "Principle Angle Spectroscopic Ellipsometry Utilizing a Rotating Analyzer," Appl. Opt., 21, 2972 (1982).
22. R.W. Stobie, B. Rao and M.J. Dignam, "Analysis of a Novel Ellipsometric Technique with Special Advantages for Infrared Spectroscopy," J. Opt. Soc. Am., 65, 25 (1975).
23. G.A. Candela and D. Chandler-Horowitz, "An Ellipsometry System for High Accuracy Metrology of Thin Films," SPIE Vol.490 Integrated Circuit Metrology II, 1984.
24. N.J. Sullo and D.T. Moore, "Measurement of Absolute Gradient-Index Profiles Using Modulation Ellipsometry," Appl. Opt., 23, 1765 (1984).
25. N.J. Sullo, "Measurement of Absolute Refractive Index Profiles in Gradient Index Materials Using Modulation Ellipsometry," Master's Thesis, University of Rochester, Institute of Optics, 1982.
26. J.L. Lauer, N. Marxer and W.R. Jones, Jr., "Ellipsometric Surface Analysis of Wear Tracks Produced by Different Lubricants," to be published in ASLE Transactions.
27. J.L. Lauer and N. Marxer, "Ellipsometric Film Thickness," to be published in Instrument Society of America.
28. Y. Yorieume, "Method for Numerical Inversion of the Ellipsometry Equation for Transparent Films," J. Opt. Soc. Am., 73, 888 (1983).
29. D. Charlot and A. Maruani, "Ellipsometric Data Processing: An Efficient Method and an Analysis of the Relative Errors," Appl. Opt., 14, 220 (1975).

30. F.L. McCrackin, "A Fortran Program for Analysis of Ellipsometer Measurements," NBS Technical Note 479, 1969.
31. W.D. Jackson, Classical Electrodynamics, John Wiley & Sons, Inc., New York, 1975.
32. F. Vasicek, "Optical Study of a Thin Absorbing Film on a Metal Surface," in "Ellipsometry in Measurement of Surfaces and Thin Films," Symposium Proceedings, Washington, 1963.
33. G.F. Leberknight and B. Lustman, "An Optical Investigation of Oxide Films on Metals," J. Opt. Soc. Am., 29, 59 (1939).
34. J.T. McCartney and S. Ergun, "Optical Properties of Graphite and Coal," Proceedings of the Third Conference on Carbon, held at the University of Buffalo, New York, 1957 (Pergamon Press Ltd., London, 1959).
35. M.E. Pedinoff and O.M. Stafstudd, "Multiple Angle Ellipsometric Analysis of Surface Layers and Surface-Layer Contaminants," Appl. Opt., 21, 518 (1982).
36. H. Senfleben and E. Benedict, Ann. der Phys., 54, 65 (1917).
37. R.H. Mueller, "Definitions and Conventions in Ellipsometry," Surface Science, 16, 14 (1969).
38. E. Stiller, "Phase Conventions in Thin Film Optics and Ellipsometry," Appl. Opt., 23, 3036 (1984).
39. M. Born and E. Wolf, Principles of Optics, 6th ed., Pergamon Press, New York, 1980.
40. R.L. Burden, J.D. Faires and A.C. Reynolds, Numerical Analysis, PWS, Boston, 1981.

## APPENDIX A

### SOME DEFINITIONS

The reading of the ellipsometry literature is often frustrating. It is practically impossible to compare results without performing some transformations, because many authors use different conventions and definitions. Muller [37] gave an excellent summary about this situation. Nine times an arbitrary choice has to be made between two alternatives. At the conference where Muller presented his paper the ellipsometry community agreed upon a particular choice, but the problem still remains.

On one hand, different sets are still used, on the other hand Stiller [38] noted, that the recommended choice for the time dependence leads to results in disagreement with experiments, when the square root of a complex number is calculated as it is done in all computers.

In the following we will state exactly the definitions used in our work so that comparison with other work is made easier. Good reference books on this topic, even though they use partly different definitions, are the books by Born and Wolf [39] and Azzam and Bashara [11].

#### Time Dependence

Light is represented by a monochromatic plane wave. We use the physicist's convention for a plane wave propagating in the  $\underline{x}$ -direction [Eq.(A.1)]:

$$e^{i(\underline{k} \cdot \underline{x} - \omega t)} \quad (A.1)$$

The variables have their conventional meaning.

### Refractive Index

The chosen time dependence leads to a positive imaginary part in the complex index of refraction. Nevertheless we still have to make a choice between the unfactored  $(n + ik)$  and the factored  $[n(1 + k)]$  version and whether the refractive index is a constant or whether it changes with the angle of incidence. We decided to use the unfactored, angle independent version for the complex index of refraction  $\hat{n}$

$$\hat{n} = n + ik \quad (A.2)$$

where  $n$  is the real refractive index and  $k$  is the extinction coefficient.

### Coordinate System

The next choice is the one for the coordinate system. We chose the direction for the axis parallel and perpendicular to the plane of incidence to be related to the direction of propagation of the plane wave according to Eq.(A.3):

$$\underline{k} \propto \underline{n}_{||} \wedge \underline{n}_{\perp} \quad (A.3)$$

where  $\underline{k}$  is the  $k$  vector and gives the direction of propagation of the plane wave,  $\underline{n}_{||}$  gives the direction of the axis in the plane of incidence (perpendicular to  $\underline{k}$ ),  $\underline{n}_{\perp}$  gives the direction of the axis perpendicular to the plane of incidence and  $\wedge$  stands for vector product.



The coordinate systems (before and after reflection, before and after refraction) are all right-handed. Figure A.1 shows the choice for the coordinate systems.

### Polarization State of Light

The electric field vector is used to define the polarization state of light. For the electric field vector components parallel and perpendicular to the plane of incidence we can write Eqs.(A.4) and (A.5), respectively. In the following, complete polarization is assumed:

$$E_{||} = e_{||} \cos(kz - \omega t + \delta_{||}) \quad (A.4)$$

$$E_{\perp} = e_{\perp} \cos(kz - \omega t + \delta_{\perp}) \quad (A.5)$$

where  $e_{||}$  and  $e_{\perp}$  are the amplitudes and  $\delta_{||}$  and  $\delta_{\perp}$  are the phase constants of the electric field vector. At a certain point in space the tip of the electric field vector describes an ellipse. There are five parameters which describe the state of polarization: the azimuth  $\theta$ , which is the angle between the major axis of the ellipse and  $\underline{n}_{||}$ , measured counterclockwise when looking towards the incoming beam; the ellipticity, which is the ratio of the length of the semi-minor axis to the length of the semi-major axis; the handedness, which describes the direction in which the terminus of the field vector traverses the ellipse; the intensity ( $\propto e_{||}^2 + e_{\perp}^2$ ), which is a measure for the size of the ellipse; and the absolute phase, which is a measure for the angle between the initial position of the electric field vector at  $t = 0$  and the major axis of the ellipse.

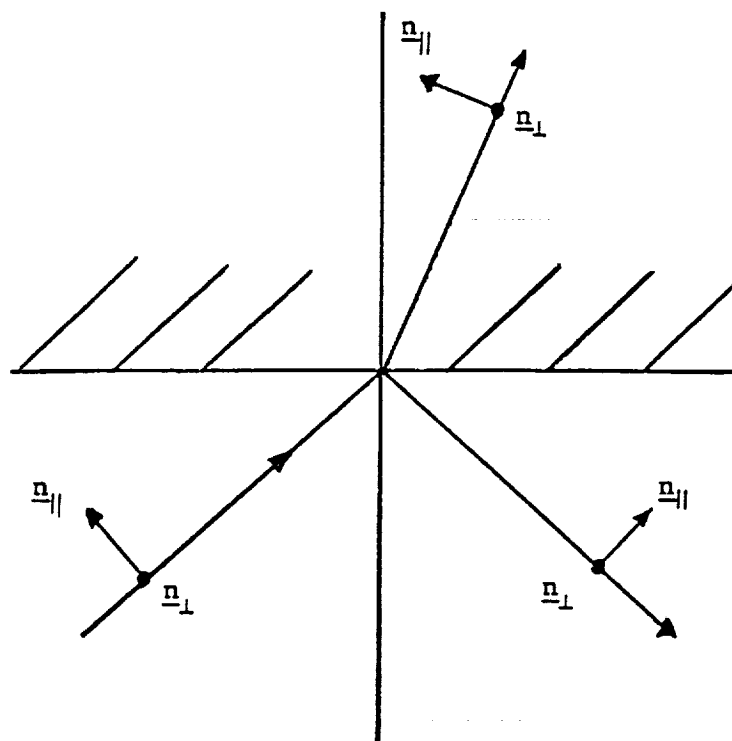


Figure A.1 Schematic of the Coordinate Systems. The plane of incidence is parallel to the page.  $\underline{n}_{||}$  is parallel to the plane of incidence and its direction is indicated for the incident, reflected and refracted beam.  $\underline{n}_{\perp}$  points always out of the page.

The absolute phase is of no importance in optics and the intensity of the light is usually not measured in ellipsometry. This leaves us with three parameters and if we combine the handedness (sign) with the (positive) ellipticity to one new (signed) "ellipticity" we will be left with two parameters. There are different ways to represent a general polarization state. We found the Poincaré-sphere representation (see below) to be the most flexible since in this representation double precision on the computer is easier to implement than in complex representations.

#### Definition of the Stokes Vector

One is led in an easy way to the Poincaré-sphere representation by starting with the so-called Stokes vector. For the electric field given by Eqs.(A.4) and (A.5) the components of the Stokes vector are defined in the following way:

$$S_0 \equiv e_{||}^2 + e_{\perp}^2 \quad (A.6)$$

$$S_1 \equiv e_{||}^2 - e_{\perp}^2 \quad (A.7)$$

$$S_2 \equiv 2e_{||}e_{\perp} \cos \delta \quad (A.8)$$

$$S_3 \equiv 2e_{||}e_{\perp} \sin \delta \quad (A.9)$$

with  $\delta \equiv \delta_{||} - \delta_{\perp}$ . Note that  $S_0^2 = S_1^2 + S_2^2 + S_3^2$ .

The zeroth component is a measure for the intensity of the wave. The first component indicates whether the light is preferentially polarized in the  $\underline{n}_{||}$  and  $\underline{n}_{\perp}$  direction. The second component is a measure for the amount of light polarized at 45 degrees to  $\underline{n}_{||}$  and  $\underline{n}_{\perp}$

and the third component is a measure for the amount of light, which is circularly polarized.

With the definitions

$$\frac{S_3}{S_0} = \sin 2\chi \quad (\text{A.10})$$

$$\frac{S_2}{S_1} = \tan 2\varphi \quad (\text{A.11})$$

we can see that  $S_1$ ,  $S_2$  and  $S_3$  are the Cartesian coordinates of a point on a sphere with radius  $S_0$  [Eqs.(A.12) to (A.14)]. This means that each point of a sphere corresponds to a certain state of polarization:

$$S_1 = S_0 \cos 2\chi \cos 2\varphi \quad (\text{A.12})$$

$$S_2 = S_0 \cos 2\chi \sin 2\varphi \quad (\text{A.13})$$

$$S_3 = S_0 \sin 2\chi \quad (\text{A.14})$$

where

$\varphi$ :  $0 \leq \varphi < 180$  - this is the angle between  $\underline{n}_{||}$  and the major axis of the ellipse

$\chi$ :  $|\tan(\chi)|$  is the ratio between the two axes of the ellipse.

For right-handed light  $\chi$  is negative and for left-handed light  $\chi$  is positive. When the electric field vector is rotating clockwise when looking towards the incoming beam, the light is by definition right-handed (in optics). This definition is just opposite to the one in physics.

### Mueller Matrices

When studying the influence of different optical components like polarizer, quarter wave plate, etc. on the polarization state of light, it is convenient to represent these components by a matrix, which acts on the Stokes vector. Then the polarization state of light

after passing some optical components can be calculated easily by multiplying the different matrices with the initial Stokes vector. The matrices which are relevant to our set-up are the ones for the polarizer, the modulator, the quarter wave plate and the sample and are derived in Appendix B.

### Fresnel Coefficients

The Mueller matrix, which represents the sample, contains two parameters  $\psi$  and  $\Delta$  (see Appendix B), which are - assuming simple models - a function of the Fresnel reflection (and transmission) coefficients. The exact form of the Fresnel coefficients, which can be derived from Maxwell's equations (see for example, Jackson [29]), will be influenced by the above choice for the coordinate systems. Because the magnetic permeabilities are usually equal to one in optics, we can write Eqs. (A.16) to (A.19) for the Fresnel coefficients:

$$r_{12}^{\perp} = \frac{n_1 \cos \alpha_1 - n_2 \cos \alpha_2}{n_1 \cos \alpha_1 + n_2 \cos \alpha_2} \quad (\text{A.16})$$

$$r_{12}^{\parallel} = \frac{n_2 \cos \alpha_1 - n_1 \cos \alpha_2}{n_2 \cos \alpha_1 + n_1 \cos \alpha_2} \quad (\text{A.17})$$

$$t_{12}^{\perp} = \frac{2n_1 \cos \alpha_1}{n_1 \cos \alpha_1 + n_2 \cos \alpha_2} \quad (\text{A.18})$$

$$t_{12}^{\parallel} = \frac{2n_1 \cos \alpha_1}{n_2 \cos \alpha_1 + n_1 \cos \alpha_2} \quad (\text{A.19})$$

where  $r_{12}^{\parallel}$ ,  $r_{12}^{\perp}$ ,  $t_{12}^{\parallel}$ ,  $t_{12}^{\perp}$  are the reflection and transmission coefficients for light polarized parallel and perpendicular to the plane of incidence, when going from medium 1 to medium 2. The refractive indices

in the two media are  $n_1$  and  $n_2$  and  $\alpha_1$  and  $\alpha_2$  are the angles between the beam and the surface normal in the two media. It can be noted, that for normal incidence, where one would expect the two reflection coefficients to be equal,  $r_{12}^{\parallel} = -r_{12}^{\perp}$ . This is due to the particular choice of our coordinate systems.

#### Definition of $\psi$ , $\Delta$ , $\rho$

When light is reflected from a surface, the electric field vector components parallel and perpendicular to the plane of incidence are affected [Eqs.(A.20) and (A.21)] (note: phasor representation for electric field),

$$e_f^{\parallel} = r_{\parallel} e^{i\Delta_{\parallel}} e_i^{\parallel} \quad (\text{A.20})$$

$$e_f^{\perp} = r_{\perp} e^{i\Delta_{\perp}} e_i^{\perp} \quad (\text{A.21})$$

where  $r_{\parallel}$ ,  $r_{\perp}$  describe the amplitude change and  $\Delta_{\parallel}$ ,  $\Delta_{\perp}$  the phase change upon reflection. With that the complex reflection coefficient  $\rho$  and the ellipsometric parameters  $\psi$  and  $\Delta$  are defined in the following way:

$$\rho \equiv \frac{r_{\parallel} e^{i\Delta_{\parallel}}}{r_{\perp} e^{i\Delta_{\perp}}} \equiv \tan \psi e^{i\Delta} \quad (\text{A.22})$$

i.e.,

$$\tan \psi = \frac{r_{\parallel}}{r_{\perp}} \quad (\text{A.23})$$

$$\Delta = \Delta_{\parallel} - \Delta_{\perp} \quad (\text{A.24})$$

## APPENDIX B

### DERIVATION OF THE MUELLER MATRICES

In the following we will discuss some tricks which make the derivation of the Mueller matrices for ideal or imperfect optical elements tractable. The derivation is given to facilitate the task for people who will continue this work.

Because we are not interested in the absolute phase, the sinusoidal time behavior and the spatial behavior, all we keep from Eqs.(A.4) and (A.5) in Appendix A is given in Eqs.(B.1) and (B.2),

$$E_{||} = e_{||} \cos \delta \quad (B.1)$$

$$E_{\perp} = e_{\perp} \quad (B.2)$$

where we eliminated the phase of the electric field component perpendicular to the plane of incidence by introducing the phase difference  $\delta = \delta_{||} - \delta_{\perp}$ . The next step is to use the phasor representation [Eqs.(B.3) and (B.4)].

$$\epsilon_{||} = e_{||} e^{i\delta} \quad (B.3)$$

$$\epsilon_{\perp} = e_{\perp} \quad (B.4)$$

where  $\epsilon_{||}$  will generally be a complex number and the electric field vectors  $E_{||}$  and  $E_{\perp}$  can be obtained by taking the real part of  $\epsilon_{||}$  and  $\epsilon_{\perp}$ , respectively. From this phasor representation it is easy to get the Stokes vectors using the following procedure [Eqs.(B.5) to (B.8)].

$$S_0 = |\epsilon_{||}|^2 + |\epsilon_{\perp}|^2 \quad (B.5)$$

$$S_1 = |\epsilon_{||}|^2 - |\epsilon_{\perp}|^2 \quad (B.6)$$

$$S_2 = 2 \operatorname{Re}(\epsilon_{\parallel} \epsilon_{\perp}^*) \quad (\text{B.7})$$

$$S_3 = 2 \operatorname{Im}(\epsilon_{\parallel} \epsilon_{\perp}^*) \quad (\text{B.8})$$

where  $\operatorname{Re}$  means the real part,  $\operatorname{Im}$  the imaginary part and  $*$  is the complex conjugate.

All the azimuths of the optical components, the Stokes vector and the Mueller matrices are given with respect to a coordinate system  $K$ , which has its axes along  $\underline{n}_{\parallel}$  and  $\underline{n}_{\perp}$ . Because it is usually simpler to derive the Mueller matrices in a special coordinate system  $K'$  (e.g., transmission axis of the polarizer coincides with one of the axes), which is rotated by  $\theta$  with respect to  $K$  [all angles are measured counterclockwise when looking towards the source starting from the plane of incidence ( $\underline{n}_{\parallel}$ )], it is useful to know how we can transform the Mueller matrix given in  $K'$  to the one in  $K$ . It can be found, that

$$\underline{S} = \underline{T}^{-1} \underline{S}' \underline{T} \quad (\text{B.9})$$

where  $\underline{S}$  and  $\underline{S}'$  are the Stokes matrices in  $K$  and  $K'$ , respectively and  $\underline{T}$  is the matrix, which transforms the Stokes vector in  $K$  to the Stokes vector in  $K'$ .  $\underline{T}^{-1}$  is the inverse matrix to  $\underline{T}$ .

The transformation matrix  $\underline{T}$  is given in Eq. (B.10):

$$\underline{T} = \begin{bmatrix} 1 & 0 & 0 & 0 \\ 0 & \cos 2\theta & \sin 2\theta & 0 \\ 0 & -\sin 2\theta & \cos 2\theta & 0 \\ 0 & 0 & 0 & 1 \end{bmatrix} \quad (\text{B.10})$$



The procedure to find the Mueller matrix is then the following:

1. The effect of the optical element on the phasor is written down in a coordinate system, where the relationship is simple.
2. The linear relationship between the final and initial Stokes vector components is derived. This gives the Stokes matrix in  $K'$ .
3. Using Eqs(A.9) and (A.10) the general representation of the optical element in  $K$  is calculated.

### Polarizer

If the polarizer has its transmission axis parallel to  $\underline{n}_{||}$ , the phasor after the polarizer is given by Eqs.(B.11) and (B.12),

$$\epsilon_f^{||} = P \cdot \epsilon_i^{||} \quad (B.11)$$

$$\epsilon_f^{\perp} = S \cdot \epsilon_i^{\perp} \quad (B.12)$$

where  $P$  is the amplitude transmission for light polarized along the plane of polarization and  $S$  is the one perpendicular to the plane of polarization. When the angle between the transmission axis of the polarizer and the plane of incidence ( $\underline{n}_{||}$ ) is  $\beta$ , then the Stokes matrix for the polarizer will be

$$\underline{P} = \frac{1}{2} P^2 \begin{bmatrix} u & v \cos 2\beta & v \sin 2\beta & 0 \\ v \cos 2\beta & u(\cos 2\beta)^2 + w(\sin 2\beta)^2 & \cos 2\beta \sin 2\beta(u - w) & 0 \\ v \sin 2\beta & \cos 2\beta \sin 2\beta(u - w) & u(\sin 2\beta)^2 + w(\cos 2\beta)^2 & 0 \\ 0 & 0 & 0 & w \end{bmatrix} \quad (B.13)$$

where  $u = 1 + \left(\frac{S}{P}\right)^2$ ,  $v = 1 - \left(\frac{S}{P}\right)^2$  and  $w = 2 \frac{S}{P}$ . For an ideal polarizer  $P = 1$  and  $S = 0$ .

### Modulator

The Faraday modulator turns the plane of polarization by an angle  $\mu$ . This is just the opposite of calculating the Stokes vector in a coordinate system, which is turned by an angle  $\mu$ . Therefore the modulator matrix corresponds to the inverse matrix  $\underline{T}^{-1}$ . This gives for the modulator

$$\underline{M} = \begin{bmatrix} 1 & 0 & 0 & 0 \\ 0 & \cos 2\mu & -\sin 2\mu & 0 \\ 0 & \sin 2\mu & \cos 2\mu & 0 \\ 0 & 0 & 0 & 1 \end{bmatrix} \quad (\text{B.14})$$

### Compensator

If the compensator has its fast axis parallel to  $\underline{n}_{||}$ , the phasor after the compensator is given by Eqs.(B.15) and (B.16),

$$\epsilon_f^{||} = F \epsilon_i^{||} \quad (\text{B.15})$$

$$\epsilon_f^{\perp} = S e^{i\delta} \epsilon_i^{\perp} \quad (\text{B.16})$$

where  $F$  is the amplitude transmission for light polarized parallel to the fast axis,  $S$  is the amplitude transmission for light polarized parallel to the slow axis and  $\delta$  is the phase difference introduced. The Stokes matrix for a compensator with an azimuth (angle between  $\underline{n}_{||}$  and the fast axis of the compensator) of  $\tau$  is then found to be

$$\underline{C} = \frac{1+T}{2} \begin{bmatrix} 1 & q \cos 2\tau & q \sin 2\tau & 0 \\ q \cos 2\tau & (\cos 2\tau)^2 - p(\sin 2\tau)^2 & \sin 2\tau \cos 2\tau(1-p) & -r \sin 2\tau \\ q \sin 2\tau & \sin 2\tau \cos 2\tau(1-p) & (\sin 2\tau)^2 + p(\cos 2\tau)^2 & r \cos 2\tau \\ 0 & r \sin 2\tau & -r \cos 2\tau & p \end{bmatrix} \quad (B.17)$$

where

$$T = \frac{S}{F} \quad (B.18)$$

$$q = \frac{1-T^2}{1+T^2} \quad (B.19)$$

$$p = \frac{2T}{1+T^2} \cos \delta \quad (B.20)$$

$$r = \frac{2T}{1+T^2} \sin \delta \quad (B.21)$$

For an ideal quarter-wave plate we have  $F=S=1$  and  $\delta = \frac{\pi}{2}$ .

### Sample

To measure the effect of the sample on the polarization state of light upon reflection from a sample is the actual purpose of the ellipsometer. The change of the phasors is described by Eqs.(B.22) and (B.23)

$$e_{\parallel}^f = r_{\parallel} e^{i\Delta} e_{\parallel}^i \quad (B.22)$$

$$e_{\perp}^f = r_{\perp} e^{i\Delta} e_{\perp}^i \quad (B.23)$$

where  $r_{||}$ ,  $r_{\perp}$  are the amplitude changes and  $\Delta_{||}$ ,  $\Delta_{\perp}$  are the phase changes of the electric field vector components upon reflection. From this we find the sample matrix

$$S = \begin{bmatrix} r_{||}^2 + r_{\perp}^2 & r_{||}^2 - r_{\perp}^2 & 0 & 0 \\ r_{||}^2 - r_{\perp}^2 & r_{||}^2 + r_{\perp}^2 & 0 & 0 \\ 0 & 0 & 2r_{||}r_{\perp} \cos \Delta & -2r_{||}r_{\perp} \sin \Delta \\ 0 & 0 & 2r_{||}r_{\perp} \sin \Delta & 2r_{||}r_{\perp} \cos \Delta \end{bmatrix} \quad (B.24)$$

or

$$S = \frac{r_{\perp}^2}{(\cos 2\psi)^2} \begin{bmatrix} 1 & -\cos 2\psi & 0 & 0 \\ -\cos 2\psi & 1 & 0 & 0 \\ 0 & 0 & \sin 2\psi \cos \Delta & -\sin 2\psi \sin \Delta \\ 0 & 0 & \sin 2\psi \sin \Delta & \sin 2\psi \cos \Delta \end{bmatrix} \quad (B.25)$$

where only the phase difference  $\Delta$  [Eq. (B.26)] enters

$$\Delta = \Delta_{||} - \Delta_{\perp} \quad (B.26)$$

Equation (B.25) is written in such a way that the dependence on the amplitude ratio [Eq. (B.27)]

$$\tan \psi = \frac{r_{||}}{r_{\perp}} \quad (B.27)$$

Here  $\psi$  and  $\Delta$  are the basic ellipsometric parameters, which will be determined experimentally and allow the calculation of film

thicknesses and optical constants;  $\psi$  and  $\Delta$  depend on the sample, the medium, the wavelength and the angle of incidence.

## APPENDIX C

### DESCRIPTION OF OPTICAL COMPONENTS

#### Light Source

Several lasers were used in our work. The one which proved to be most useful was a CW Radiation laser, which supplies a monochromatic (632.8 nm), polarized 25 mW beam of light.

#### Polarizer

We used two sets of polarizers. The first set consisted of air-spaced calcite polarizing prism made by Optics for Research (PL-10); the second set consisted of film polarizers. The calcite polarizers have a lower extinction ratio (= ratio between the intensity transmitted through two crossed polarizers and the intensity transmitted through two polarizers having their transmission axes parallel), but a larger beam deviation (see Table C.1) than the film polarizers. For high resolution measurements the beam deviation of the polarizers causes the image of the sample to wander on the detector. The movement was less for the film polarizer and using them a resolution of 20  $\mu\text{m}$  could be achieved.

#### Quarter-Wave Plate

The quarter-wave plate (at 632.8 nm) was purchased from Oriel Corporation and is a zero order quartz, with  $1/300 \lambda$  retardation tolerance, anti-reflective coating, an aperture of 14.5 mm and mounted in a holder. The beam deviation is 2 to 5 arc seconds.

TABLE C.1

EXTINCTION RATIO AND BEAM DEVIATION FOR A  
CALCITE AND FILM POLARIZER

Calcite polarizer	Extinction Ratio $10^{-5}$ to $10^{-6}$	Beam Deviation 3 arc min
Film polarizer	a few $10^{-4}$	30 arc sec

### Faraday Modulator

As the name suggests, the Faraday modulator makes use of the Faraday effect, i.e., when light passes through special material (e.g., Hoya FR-5 glass, a terbium doped silicate) and a magnetic field is applied along the direction of propagation, the plane of polarization of linearly polarized light is rotated by an angle  $\alpha$ , which is proportional to the magnetic field  $H$  and the length of the glass  $l$ , the proportionality constant  $V$  being called the Verdet constant [Eq.(C.1)]:

$$\alpha = V \cdot H \cdot l \quad (C.1)$$

The Faraday modulator consists of a glass rod inside a concentric solenoid. We have two pieces of glass. One is 100 mm long, the other 31 mm, both have a diameter of 6.35 mm and the parallelism of the end faces is within 30 arc seconds. The Verdet constant of the glass is specified to be  $0.23 \frac{\text{arc min}}{\text{Oe cm}}$  at  $\lambda = 632.8 \text{ m}$ . The glass is mounted rigidly (press fit) inside a plastic tube. No contact is made with the end faces.

We made one coil for each of the two glass pieces. For the short one (for example) we have an inner diameter of 11 mm, a length of 58 mm and about 2600 windings.

By applying an AC (typically 500 Hz) current of approximately 0.5 A we produce a time varying magnetic field, which turns the plane of polarization of linearly polarized light back and forth by approximately one degree. The modulation  $\mu_0$  should be large to cause a large AC signal on the detector, but it should not be too large so that we still can expand  $\sin(\mu_0 \sin \omega t) \approx \mu_0 \sin \omega t$ .



### Filter

A filter is in front of the detector to keep out most of the ambient light. The filter has a peak (71% transmission) at 632.4 nm with a full width at half maximum of 2.6 nm.

### Detector

The detector used for most of the work is a UDT-455 PHOTOPS detector/amplifier combination from United Detector Technology. These detectors have ultrasensitive silicon photodiodes with a spectral range from 350 to 1100 nm and the responsivity at 632.8 nm is approximately .35 Ampere per Watt. We operated the detector in the photovoltaic mode and different feedback loops made it possible to work at different light levels.

### Sample Stage

The sample is mounted on a stage, which allows for translation in the x- and y-direction (= plane of the surface) with a Motor Mike actuator (Oriel Corporation) with position readout. The position readout is fed to our electronics boards, analyzed and transmitted to the computer. A fine pitch screw running in a precision threaded nut, combined with a 485:1 gear reduction, makes a .02 micron resolution possible (disregarding the encoder signals). There is another manually actuated translation stage in the z-direction normal to the surface for alignment purposes. The sample can be rotated around the x- and y-direction in order to reflect the incident beam to the detector. The holders built and used are of different designs depending on the samples studied (e.g., small metal samples or computer disks). The only requirement is, that the sample is very rigidly attached to the stage.

### Rotation Stage

The rotation stages for the polarizer and analyzer are DC motor driven stages (UR 80 CC and UR 100 CC from Klinger Scientific) with encoder for position verification (.01 degree resolution). The quadrature signals from these two stages are connected to our boards and the position is determined electronically. The rotation stage for the quarter-wave plate is mounted in an Oriel rotation stage (manually driven). The accuracy of the position readout is .1 degree over the full 360 degrees and .01 degree over a range of 16 degrees (for relative changes).

### Variable Angle of Incidence

We have the means of varying the angle of incidence using a stepping motor. The range is from approximately 25 degrees to 80 degrees. The fact that the smallest possible angle of incidence is 25 degrees is no limitation, because at small angles  $\psi$  is always close to 45 degrees and  $\Delta$  is always close to 180 degrees. The action is happening at larger angles and therefore an angle of incidence as large as possible is desirable. An upper limit is given by the fact that for very large angles the laser light covers too big an area on the sample.

The error in the angle of incidence comes entirely from the positioning of the sample; the reproducibility in setting the two optical arms where the optical components are tightly attached is excellent and does not contribute. We have chosen a very long arm

on the detector side to position the sample as accurately as possible.  
The error was estimated to be a few hundredths of a degree.

## APPENDIX D

### DESCRIPTION OF ELECTRONIC COMPONENTS AND BOARDS

In this appendix we describe the principle of a phase-locked loop and several electronic instruments. The counter-boards and the computer control are home-made. Because the counterboards determine the maximum achievable precision of the ellipsometer, they are described in some detail. A complete description of the computer control would take too much space and, therefore, only an outline is given.

#### Principle of Phase-Locked Loop

The principle of the phase-locked loop is best understood by locking at the PSMA set-up. With the modulator turned off (no current) and the polarizer set at an arbitrary azimuth, the light intensity at the detector will be a minimum for the transmission axis of the analyzer parallel to the semi-minor axis of the polarization ellipse.

Rotating the analyzer back and forth would have the same effect as turning on the modulator. As can be seen from Figure D.1 for a modulation around the minimum, light seen by the detector will be modulated with a frequency  $2f$ , whereas away from the minimum it will be modulated with a frequency  $f$ . This modulation is in both cases superimposed on a DC component.

Because the light intensity at the fundamental frequency to the right and left of the minimum is 180 degrees out of phase, it can be used to drive the analyzer back to the minimum position (lock-in).

Figures D.2 and D.3 show photographs of the intensity at and close to the minimum, respectively.

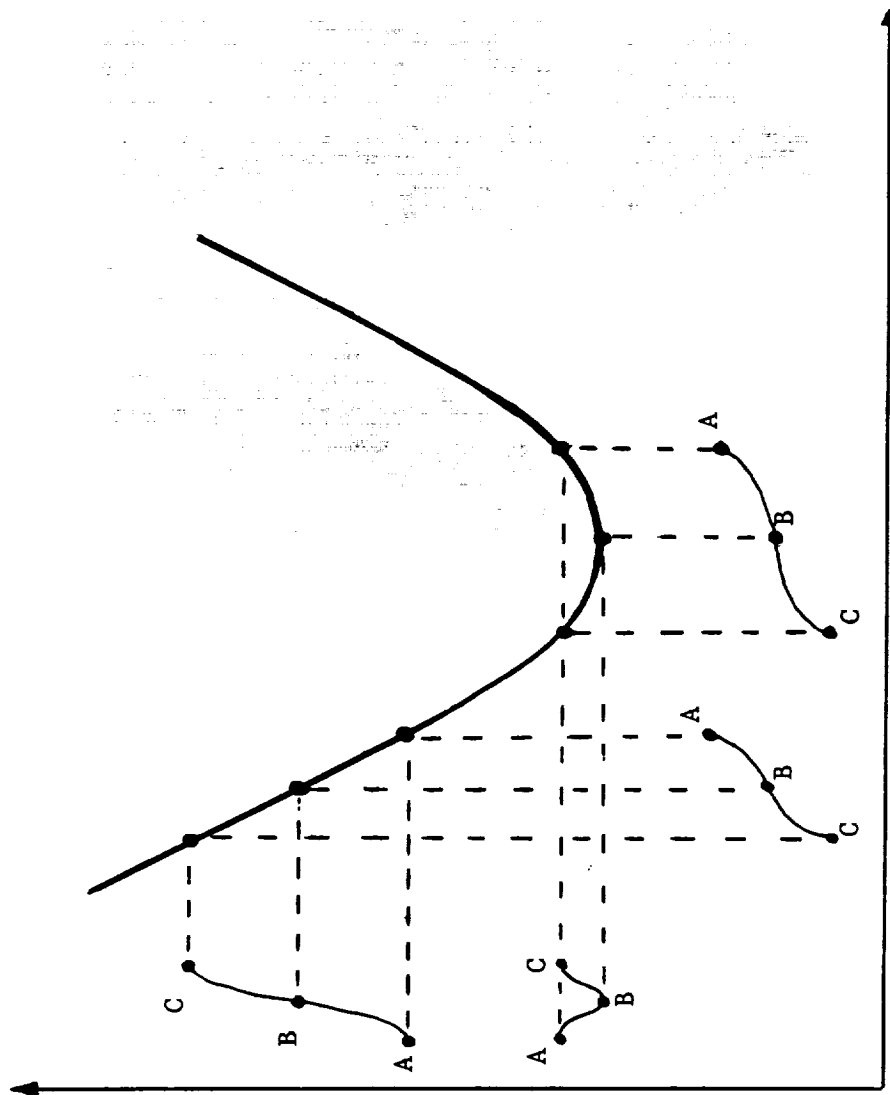


Figure D.1.1 Intensity Modulation Caused by Moving the Analyzer at the Minimum and Away from the Minimum

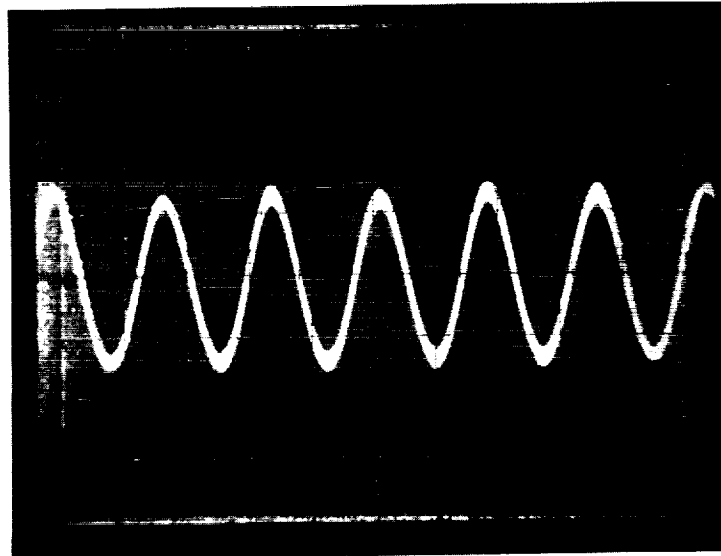


Figure D.2 Second Harmonic of the Light Intensity.  
The ellipsometer is locked in.

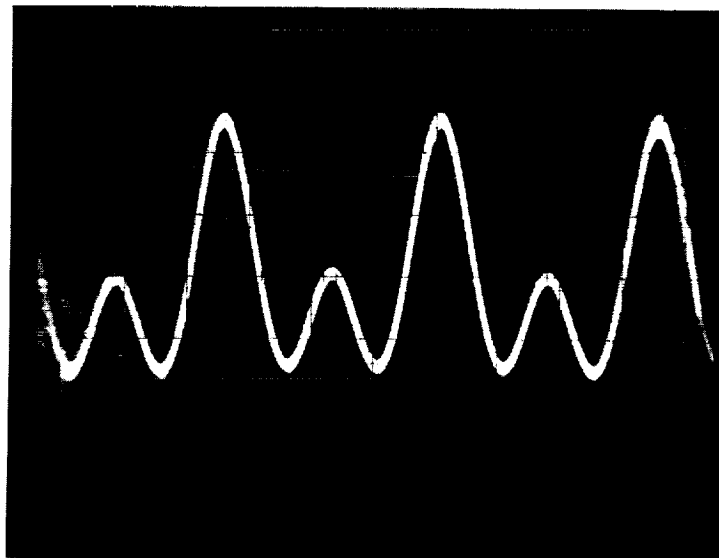


Figure D.3 First and Second Harmonic of the Light Intensity. Analyzer azimuth is 0.20 degrees away from the minimum.

### Phase-Locked Amplifier

The phase locked amplifier used is a Dynatrac 391 A from Ithaco with a maximum sensitivity of  $1 \mu\text{V}$ . With the card used the lock-in frequency can lie between 100 and 10,000 Hz.

### Oscillator

The output of a frequency generator (usually a sine wave at 500 Hz) is fed both to the reference input of the lock-in amplifier and via a power amplifier to the Faraday coil.

### Counter Boards

The (relative) position of the translation and rotation stages is determined by our so-called counter boards. The position readout should be as accurate as possible, because it determines the ultimate precision of the ellipsometer. The signals we receive from the optical encoders are quadrature signals (Figure D.4). For continuous motion in one direction there will be two rectangular waves 90 degrees out of phase. In the reverse direction the two waves will be 270 degrees out of phase. This is all the information we have and need to determine the relative position (relative to a certain starting point) of the translation stage or the rotation stages, if we know how much the stage is moved per pulse.

The two signals A and B are differentiated (electronically), so that we get a pulse for each edge (dA and dB). If the stage is moving in one direction X [Eq.(D.1)] will produce a pulse at each edge, if the stage is moving in the other direction Y [Eq.(D.2)] will produce a pulse at each edge:



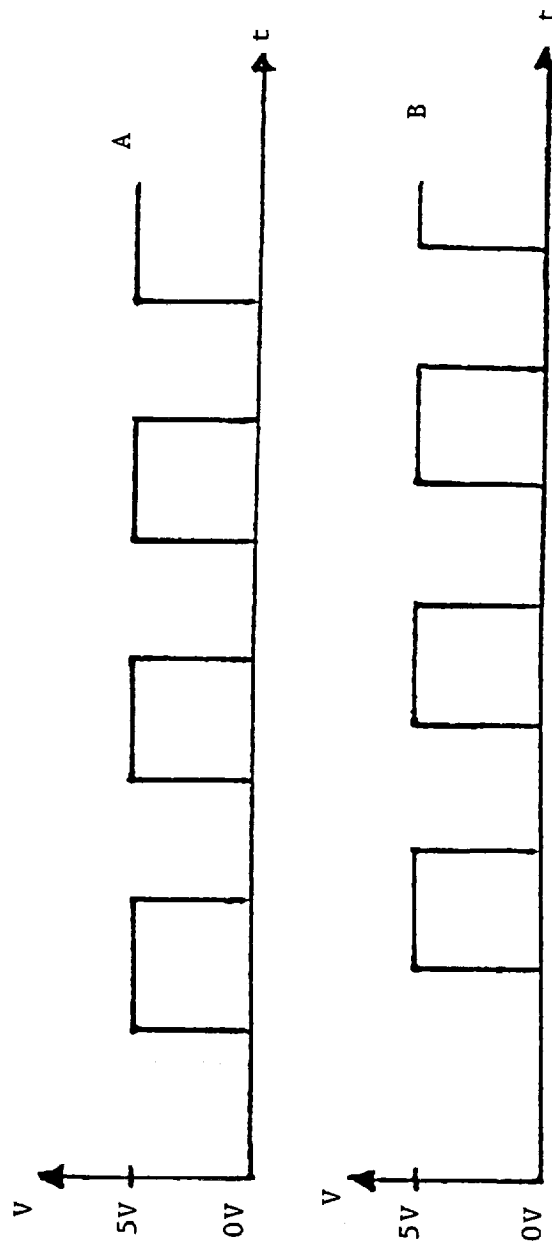


Figure D.4 Shape and Phase Relationship of the Two Quadrature Signals A and B

$$X = (\bar{A} \vee dB) \vee (dA \wedge B) \vee (A \wedge \bar{dB}) \vee (\bar{dA} \wedge B) \quad (D.1)$$

$$Y = (\bar{A} \wedge \bar{dB}) \vee (dA \wedge \bar{B}) \vee (A \wedge dB) \vee (\bar{dA} \wedge B) \quad (D.2)$$

where the bar above A, B, dA and dB means the inverted signal (5V $\leftrightarrow$ 0V),  $\wedge$  stands for logical AND and  $\vee$  stands for logical OR. These two signals are fed to the first of five cascaded BCD (binary coded decimal) counters (SN74192). At the output of each of these counters one digit is available. The four bits representing a digit are connected both to a digital display unit (SN 7447 BCD to seven segment decoder/driver and DL707 common anode seven segment display) and to octal D-type transparent latches (SN74373). Every time a pulse (from the computer) is given to the enable input of the latch, the data at the input is stored in the latch and made available at the output.

The four bits of the least significant digit are fed to the inputs A of four 1 of 8 data selectors/multiplexers (SN 94151). The four bits of the second least significant digit are fed to the inputs B of the four multiplexers and so on for all five digits. Then depending on the address at the data select input of the multiplexers, the four bits of one of the five digits are available at the output of the multiplexers and can be transmitted to the computer.

### Control Electronics

In the normal operation of the ellipsometer one stage is moved (polarizer, analyzer or translation stage) and another stage (polarizer or analyzer) is in the feedback loop and turned automatically in such a way that the intensity at the fundamental frequency becomes

zero. The ellipsometer can be operated both manually (where one stage is moved, another stage nulls the signal, and the counters give the positions of all the stages) and computer controlled. The manual mode is usually used for start-up or testing; the normal operation is the computer controlled one.

It would take too long to explain the detailed realization of the four boards, which are needed to operate the ellipsometer. An outline of the capabilities is given below. Extensive use was made of logic gates (AND, OR, INVERTER, etc.), latches (where bits can be stored), multiplexers (where one of several input lines - selected by the address at the data select input - can be directed to the output), demultiplexers [where one of several output lines - selected by the address at the data select input - can be made low (0 Volt) whereas all the other lines are high (5 Volt)], counters and other components.

An IBM - PC computer with an input/output board (DT2808 from DATA TRANSLATION) is used to interface to the ellipsometer. The DT2808 board has 16 digital I/O-lines besides some A/D and D/A channels which are not used for the ellipsometer. Eight lines are used to control the ellipsometer (output) and eight lines are used for collecting the data (input). Setting the bits at the output and reading the input lines is done by BASIC subroutines and a BASIC program controls the operation of the ellipsometer.

In the following we list what we can do with our BASIC subroutines:

1. We can choose the direction in which the different stages move. The direction chosen for the stage in the feedback loop determines whether the ellipsometer locks in at a minimum or a maximum of the intensity.
2. We can select the stage (analyzer or polarizer) which should be connected to the lock-in amplifier.
3. We can select the stage which should be driven by a DC motor (polarizer, analyzer or translation stage).
4. We can drive one stage and the stage in the feedback-loop will lock-in if so desired. The driven stage will move until one of the two stages as selected has moved by a predetermined amount. Then the DC motor is turned off automatically and a bit set at one of the input lines of the computer signals that a reading can be taken.
5. We can read the angles of the rotation stages and the position of the translation stage into the computer.

Using these commands the ellipsometer can be operated in the three modes as discussed in Chapter 4.

The data collected are transmitted via a RS-232 connector to our larger laboratory computer, where the UNIX operating system and a Fortran compiler are available. The IBM-PC is only used for controlling the ellipsometer and data acquisition, all the calculations are done on the larger Starlab computer.

## APPENDIX E

### COMPUTER PROGRAMS

In the following we will mention features of some of the computer programs used. No listing is given.

#### Lock.go

Lock.go simulates the operation of the ellipsometer. From up to ten optical elements (including a sample) all except one are set at a certain azimuth and the program determines the azimuth of the remaining one such that the intensity at the fundamental frequency, which is found by multiplying the Mueller matrices with the initial Stokes vector, is equal to zero. In addition intensities (DC, first and second harmonic) can be calculated for arbitrary settings of the components. This program is particularly useful in checking the influence of imperfections in optical components and also in finding the settings where the ellipsometer gives the most accurate results.

#### Elli.go

Elli.go calculates optical constants and film thickness(es) for measured  $\psi$  and  $\Delta$ , or  $\psi$  and  $\Delta$  for given optical constants, film thickness(es), angle of incidence, etc.

Table E.1 shows what some of the subroutines in `elli.go` can do. CTABLE, CNS, CD, CND and CNK are subroutines using algorithms described by McCrackin [32]. Their implementation has to be done with extreme care, because it has to be made sure that the computer selects the right solution when taking a square root or logarithm of a complex

TABLE E.1  
INPUT AND OUTPUT OF SOME OF THE SUBROUTINES OF THE PROGRAM ELLI.GO\*

Subroutine	Input	Output	Number of Films
CTABLE	$\lambda, \alpha, n_M, \hat{n}_s, \hat{n}_F, t_{F_i}, \psi, \Delta$ $i = 1, 50$	$\psi, \Delta$	Up to 50
CNS	$\lambda, \alpha, n_M, \psi, \Delta$	$\hat{n}_s$	None
CD	$\lambda, \alpha, n_M, \hat{n}_s, \hat{n}_F, \psi, \Delta$	$t_F$	One
CND	$\lambda, \alpha, n_M, \hat{n}_s, k_F, \psi, \Delta$	$n_F, t_F$	One
CNK	$\lambda, \alpha, n_M, \hat{n}_s, t_F, \psi, \Delta$	$\hat{n}_F = n_F + ik_F$	One
SEARCH	$(\psi_i, \Delta_i, \alpha_i)$	You decide	Up to 50

- \*  $\lambda$  = wavelength  
 $\alpha$  = angle of incidence  
 $n_M$  = real refractive index (medium)  
 $\hat{n}_s$  = complex refractive index (substrate)  
 $\hat{n}_F$  = complex refractive index (film)  
 $n_F$  = real refractive index (film)  
 $k_F$  = extinction coefficient (film)  
 $\psi, \Delta$  = ellipsometric parameters

number. Many times this is not the case and special subroutines have to be written to correct for that. Subroutine SEARCH avoids these problems (partly). It is based on a least square fitting procedure:  $\psi$  and  $\Delta$  which were measured at one or more angles of incidence are input, a model is assumed (e.g., two films on a substrate) and (some of the) refractive indices or film thickness(es) are varied within intervals until the measured and calculated  $\psi$  and  $\Delta$  are closest together. Different weight factors can be included to take into account that the error in  $\Delta$  is usually larger than the error in  $\psi$ .

Subroutine SEARCH is especially useful in multiple angle of incidence measurements, but it can also do what CNS, CD, CND and CNK do and has been used for almost all the thin film calculations.

#### Pd.go

Pd.go determines  $\psi$  and  $\Delta$  and the offsets of the polarizer and analyzer readings as explained below. Because it is the most important program used to find  $\psi$  and  $\Delta$ , it is explained in some detail. When the instrument is operated without the quarter wave plate, two modes of operation are possible: PMSA or PSMA. In both cases an analysis shows that the polarizer angle  $\beta$  and the analyzer angle  $\alpha$  are related by an equation like Eq.(E.1),

$$\tan 2Y = \frac{2 \cos \Delta \tan \psi \tan X}{(\tan \psi)^2 - (\tan X)^2} \quad (\text{E.1})$$

where

$X = \beta, Y = \alpha$  for PSMA

$Y = \beta, X = \alpha$  for PMSA.

To obtain the ellipsometric parameters  $\psi$  and  $\Delta$  from a number of measured (analyzer, polarizer) pairs, a least square fit to Eq.(E.1) can be performed.

Because there is no absolute position encoder in our rotation stage we have to reset our counter boards at the beginning of an experiment using the dials on the rotation stages. This is not very accurate of course and, therefore, we use Eq.(E.1) to find the exact analyzer and polarizer angles in addition to the ellipsometric parameters  $\psi$  and  $\Delta$ .

We note that the measured polarizer angles  $\beta_i^m$  and analyzer angles  $\alpha_i^m$  have a constant offset  $\beta_o$  and  $\alpha_o$ , respectively:

$$\beta_i = \beta_i^m + \beta_o \quad (E.2)$$

$$\alpha_i = \alpha_i^m + \alpha_o \quad (E.3)$$

where  $\alpha_i$  and  $\beta_i$  are the true angular positions of the two rotation stages. These two "true" angles should fulfill Eq.(E.1). We then get (for PSMA, e.g.):

$$\tan\left(2(\alpha_i^m + \alpha_o)\right) = 2 \cdot \cos \Delta \frac{\tan \psi \tan(\beta_i^m + \beta_o)}{(\tan \psi)^2 - (\tan(\beta_i^m + \beta_o))^2} \quad (E.4)$$

or

$$\alpha_i^m + \alpha_o = \frac{1}{2} \tan^{-1} \left( 2 \cos \Delta \frac{\tan \psi \tan(\beta_i^m + \beta_o)}{(\tan \psi)^2 - (\tan(\beta_i^m + \beta_o))^2} \right) \quad (E.5)$$



The four unknowns  $\alpha_o$ ,  $\beta_o$ ,  $\tan \psi$  and  $\cos \Delta$  are now determined by a least square fit. That means that  $E$  [Eq.(E.6)] should become a minimum with respect to the variables  $\alpha_o$ ,  $\beta_o$ ,  $\tan \psi$  and  $\cos \Delta$ :

$$E = \sum \left( 2(\alpha_i^m + \alpha_o) - \tan^{-1} \left( 2 \cos \Delta \frac{\tan \psi \tan(\beta_i^m + \beta_o)}{(\tan \psi)^2 - (\tan(\beta_i + \beta_o))^2} \right) \right)^2 = \sum F_i^2 \quad (E.6)$$

where the summation includes all the measured (analyzer, polarizer) pairs. Defining

$$\gamma = 2 \cos \Delta$$

$$\delta = \tan \psi$$

$$F_i: \text{ see Eq. (E.6)}$$

$$g_i = \gamma \frac{\delta \tan(\beta_i^m + \beta_o)}{\delta^2 - (\tan(\beta_i^m + \beta_o))^2}$$

$$d_i = \delta^2 - (\tan(\beta_i + \beta_o))^2$$

and setting the derivatives of  $E$  with respect to the four unknowns equal to zero gives us the following four nonlinear equations, where linear dependent terms have been eliminated:

$$\sum F_i = 0 \quad (E.7)$$

$$\sum \frac{F_i}{1 + g_i^2} = 0 \quad (E.8)$$

$$\sum \frac{F_i g_i}{(1 + g_i^2) d_i} = 0 \quad (E.9)$$

$$\sum \frac{F_i}{(1+g_i^2)d_i(\cos(\beta_i^m + \beta_o))^2} \left[ 1 + \frac{2g_i^2 d_i}{\gamma^2 \delta^2} \right] \quad (E.10)$$

This system of equations can be solved using Newton's method for non-linear systems (see Burden, Faires and Reynolds [40]).

We can write Eqs.(E.7) to (E.10) as:

$$\underline{F}(\underline{x}) = 0 \quad (E.11)$$

where

$$\underline{x} = \begin{pmatrix} \alpha_o \\ \gamma \\ \delta \\ \beta_o \end{pmatrix} \quad \text{and} \quad \underline{F} = \begin{pmatrix} F_1 \\ F_2 \\ F_3 \\ F_4 \end{pmatrix}$$

The  $F_i$  ( $i=1,4$ ) are the four functions on the left sides of Eq.(E.7) to Eq.(E.10). Equation (E.11) will be true for the correct solution of  $\alpha_o$ ,  $\gamma$ ,  $\delta$ ,  $\beta_o$ . If we start with some value  $\underline{x}$  in the neighborhood of the correct solution, the iteration

$$\underline{x}^{(k)} = \underline{x}^{(k-1)} - \underline{J}^{-1}(\underline{x}^{(k-1)}) \underline{F}(\underline{x}^{(k-1)}) \quad (E.12)$$

will converge to the true solution. Here  $\underline{x}^{(k)}$  is  $\underline{x}$  after the  $k$ th iteration and  $\underline{J}^{-1}(\underline{x}^{(k-1)})$  is the inverse of the Jacobian matrix  $\underline{J}$

$$\underline{J} = \begin{pmatrix} \frac{\partial F_1}{\partial \alpha_o} & \frac{\partial F_1}{\partial \gamma} & \frac{\partial F_1}{\partial \delta} & \frac{\partial F_1}{\partial \beta_o} \\ \frac{\partial F_2}{\partial \alpha_o} & \frac{\partial F_2}{\partial \gamma} & \frac{\partial F_2}{\partial \delta} & \frac{\partial F_2}{\partial \beta_o} \\ \frac{\partial F_3}{\partial \alpha_o} & \frac{\partial F_3}{\partial \gamma} & \frac{\partial F_3}{\partial \delta} & \frac{\partial F_3}{\partial \beta_o} \\ \frac{\partial F_4}{\partial \alpha_o} & \frac{\partial F_4}{\partial \gamma} & \frac{\partial F_4}{\partial \delta} & \frac{\partial F_4}{\partial \beta_o} \end{pmatrix} \quad (E.13)$$

The Jacobian matrix is found by differentiating E twice with respect to the four unknowns  $\alpha_o$ ,  $\gamma$ ,  $\delta$ ,  $\beta_o$ . We get very long and complicated expressions. Limited space does not permit to write it down here.

We can rewrite Eq.(E.12)

$$\underline{J} \underline{y} = \underline{F} \quad (E.14)$$

with the definition  $\underline{y} = \underline{x}^{(k-1)} - \underline{x}^{(k)}$ . Having found  $\underline{y}$ , we can calculate  $\underline{x}^{(k)}$  and repeat the above steps until convergence is reached.

This calculation provides us with  $\alpha_o$ ,  $\cos \Delta$ ,  $\tan \psi$  and  $\beta_o$ .

With suitable starting values convergence is reached very quickly and the RMS deviation between the calculated and measured analyzer azimuth (PSMA) is typically close to 0.01 degrees, the resolution of our rotation stages. Therefore, more accurate results for  $\psi$  and  $\Delta$  can only be obtained by using stages with better resolution.



1. Report No. <b>NASA CR-4012</b>		2. Government Accession No.		3. Recipient's Catalog No.	
4. Title and Subtitle  <b>Polarization Modulated Ellipsometry</b>				5. Report Date <b>September 1986</b>	
				6. Performing Organization Code	
7. Author(s)  <b>James L. Lauer and Norbert Marxer</b>				8. Performing Organization Report No.  <b>None</b>	
				10. Work Unit No.	
9. Performing Organization Name and Address <b>Rensselaer Polytechnic Institute Department of Mechanical Engineering, Aeronautical Engineering and Mechanics Troy, New York 12180-3590</b>				11. Contract or Grant No.  <b>NAG3-222</b>	
				13. Type of Report and Period Covered  <b>Contractor Report</b>	
12. Sponsoring Agency Name and Address  <b>National Aeronautics and Space Administration Washington, D.C. 20546</b>				14. Sponsoring Agency Code  <b>505-63-01 (E-3173)</b>	
15. Supplementary Notes  <b>Final report. Project Manager, William R. Jones, Jr., Materials Division, NASA Lewis Research Center, Cleveland, Ohio 44135.</b>					
16. Abstract  <b>For the investigation of the composition and thickness of thin nonuniform films on bearing and other tribological surfaces an automated ellipsometer was built, which is extremely sensitive to relative changes in thickness and composition of surface films. These changes can be seen by scanning across the surface with 20 <math>\mu</math>m lateral resolution. By measuring at different angles of incidence one can determine the film thickness and identify the material of the film by its complex index of refraction. For the analysis of organic layers on top of several metallic layers it was necessary to develop mathematical procedures to increase the absolute precision of the instrument. The ellipsometer is described in detail, and the precision is discussed. The actual performance of the ellipsometer was tested on three experiments. In the first one the composition and thickness of patches of an oxide film inside a wear track were determined. In the second the thickness of a carbon overcoat sputtered on a computer disk was measured: the carbon was identified as graphite and of random orientation. In the third the thickness of silicon oxide on top of a silicon substrate was found. Important features of this apparatus are (i) accurate settings of the polarization stages and the angle of incidence (both automated), (ii) high precision in the determination of the ellipsometric parameters without calibration prior to an experiment and (iii) very accurate scanning modes with high spatial resolution. The instrumentation and the mathematical procedures were developed here for the first time.</b>					
17. Key Words (Suggested by Author(s))  <b>Ellipsometry Tribology</b>			18. Distribution Statement  <b>Unclassified - unlimited STAR Category 74</b>		
19. Security Classif. (of this report)  <b>Unclassified</b>		20. Security Classif. (of this page)  <b>Unclassified</b>		21. No. of pages  <b>111</b>	
				22. Price*  <b>A05</b>	

